

# 1 **EpiGePT: a Pretrained Transformer model for epigenomics**

2 Zijing Gao<sup>1,#</sup>, Qiao Liu<sup>2,#,\*</sup>, Wanwen Zeng<sup>2</sup>, Wing Hung Wong<sup>2,3,\*</sup> and Rui Jiang<sup>1,\*</sup>

3 <sup>1</sup> Ministry of Education Key Laboratory of Bioinformatics, Research Department of  
4 Bioinformatics at the Beijing National Research Center for Information Science and  
5 Technology, Center for Synthetic and Systems Biology, Department of Automation, Tsinghua  
6 University, Beijing 100084, China;

7 <sup>2</sup>Department of Statistics, Stanford University, Stanford, CA 94305, USA;

8 <sup>3</sup> Department of Biomedical Data Science, Bio-X Program, Center for Personal Dynamic  
9 Regulomes, Stanford University, Stanford, CA 94305, USA;

10 \* To whom correspondence should be addressed.

11 # The first two authors contributed equally.

12 E-mail: [liuqiao@stanford.edu](mailto:liuqiao@stanford.edu), [whwong@stanford.edu](mailto:whwong@stanford.edu), [ruijiang@tsinghua.edu.cn](mailto:ruijiang@tsinghua.edu.cn)

## 13 **Abstract**

14 The transformer-based models, such as GPT-3<sup>1</sup> and DALL-E<sup>2</sup>, have achieved unprecedented  
15 breakthroughs in the field of natural language processing and computer vision. The inherent  
16 similarities between natural language and biological sequences have prompted a new wave of  
17 inferring the grammatical rules underneath the biological sequences. In genomic study, it is  
18 worth noting that DNA sequences alone cannot explain all the gene activities due to epigenetic  
19 mechanism. To investigate this problem, we propose EpiGePT, a new transformer-based  
20 language pretrained model in epigenomics, for predicting genome-wide epigenomic signals by  
21 considering the mechanistic modeling of transcriptional regulation. Specifically, EpiGePT  
22 takes the context-specific activities of transcription factors (TFs) into consideration, which  
23 could offer deeper biological insights comparing to models trained on DNA sequence only. In  
24 a series of experiments, EpiGePT demonstrates state-of-the-art performance in a diverse  
25 epigenomic signals prediction tasks as well as new prediction tasks by fine-tuning. Furthermore,  
26 EpiGePT is capable of learning the cell-type-specific long-range interactions through the self-  
27 attention mechanism and interpreting the genetic variants that associated with human diseases.  
28 We expect that the advances of EpiGePT can shed light on understanding the complex  
29 regulatory mechanisms in gene regulation. We provide free online prediction service of  
30 EpiGePT through <https://health.tsinghua.edu.cn/epigept/>.

## 31 **Introduction**

32 One of the fundamental problems in genomic study is how to decode and interpret the human  
33 genome sequences in a complex manner. Progress toward this goal is largely hindered by the  
34 vast majority of non-coding regions<sup>3</sup>. For example, it remains unclear how the genomic variants  
35 in the noncoding regions lead to malfunctions of regulatory elements by disrupting the  
36 underlying regulatory syntax of DNA<sup>4</sup>. Inspired from the field of natural language processing,  
37 there exists a natural analogy between human language and DNA sequence where texts are  
38 made of words and DNA sequence can be characterized by nucleotides or k-mers. The inherent  
39 similarities between natural language and biological sequences provide new perspectives  
40 towards better understanding the complex DNA language.

41 Recently, generative pre-trained transformer (GPT) models have achieved unprecedented  
42 success in various domains, including computer vision and natural language processing (NLP)<sup>1</sup>,  
43 <sup>5</sup>. Such pre-trained models can be readily tailored or adapted to various downstream tasks. To  
44 date, the application of generative pre-trained models in genomic study remains largely  
45 unexplored. It is noticeable that a number of machine learning-based approaches have been  
46 proposed for predicting various genomic and epigenomic signals, such as chromatin  
47 accessibility<sup>6, 7</sup>, histone modification<sup>8</sup> or chromatin interactions<sup>9, 10</sup>. However, these methods  
48 are rather scattered, with specific models designed for specific prediction tasks. It is in an urgent  
49 need to develop a foundation model to facilitate multiple genomic and epigenomic prediction  
50 tasks and unveil the universal gene regulation rules.

51 To design a genomic foundation model, it is worth noting that the existing large language

52 models (LLMs) purely rely on the language context consisting of words and sentences while  
53 the DNA sequences cannot explain all the heritable and stable changes in gene activity due to  
54 epigenetic mechanisms. In other words, the genomic foundation model based on pure DNA  
55 sequence may largely ignore the context-specific information, thus lacking mechanistic  
56 interpretation of context-specific gene regulation. For example, using transformer-based  
57 language model to decode genome sequence has been attempted by a recent work Enformer<sup>11</sup>.  
58 However, Enformer is not capable of predicting the function of sequences in new cellular  
59 contexts, which largely limits its generalization power.

60 To overcome the above limitation, we proposed EpiGePT, a new transformer-based deep  
61 learning framework, to predict genome-wide epigenomic signals by taking the mechanistic  
62 modeling of transcriptional regulation into consideration. With EpiGePT, we are able to  
63 investigate how to utilize the power of transformer-based language model to help researchers  
64 uncover how trans-regulatory factors (e.g., TFs) regulate target genes by interacting with cis-  
65 regulatory elements and further lead to changes in different chromatin states. After pretraining  
66 on a diverse panel of cell line and tissue level data from the Encode database<sup>12</sup>, EpiGePT is able  
67 to directly predict the genome-wide chromatin states in any new cellular context given the  
68 expression profile of a few hundreds of TFs or facilitate new prediction tasks (e.g., 3D genome  
69 interaction) with finetuning.

70 To the best of our knowledge, EpiGePT is the first pretrained Transformer model for  
71 epigenomics with mechanistic modeling of transcriptional regulation. EpiGePT differs from  
72 existing methods in the following three aspects. First, unlike the methods that take pure DNA  
73 sequence as input, EpiGePT additionally takes the context-specific information (e.g., TF

74 activities) as input, thus enabling genome-wide prediction power in any new cellular context.

75 Second, instead of using task-specific model to predict a single genomic and epigenomic signal,

76 EpiGePT is designed for simultaneously predicting multiple epigenomic signals of the same

77 genomic region through multi-task learning, thus improving learning efficiency and prediction

78 accuracy compared to the task-specific models. Third, many methods typically take short DNA

79 sequence (e.g., a few hundred or a thousand base pair) as input, which may not be adequate to

80 capture the complex syntax of DNA due to truncation. The long input DNA sequence (e.g.,

81 128kb) for EpiGePT greatly enhances the ability for the model to capture the long-range

82 interaction in the genome, which are crucial for understanding the gene regulation mechanism.

83 In a series of experiments, we illustrate that our method is superior to existing methods in a

84 various tasks of chromatin states prediction, as well as the variant effect prediction. We also

85 show that the self-attention mechanism greatly helps unveil the complex code in the

86 conformation of long-range chromatin interactions, such as promoter-enhancer interactions and

87 promoter-silencer interactions. EpiGePT is an example of how transformer-based language

88 model and large-scale pretrain can be used in genomics research to provide biological insights.

89 With the help of EpiGePT model, it is expected that researchers can dissect the comprehensive

90 genomic regulatory code given the cellular context information and accelerate research findings

91 in genomic study.

## 92 **Results**

### 93 **Overview of EpiGePT model**

94 We developed a novel Transformer<sup>13</sup>-based language model named EpiGePT to predict multiple  
95 chromatin states across different cell types. EpiGePT is a language model for cross-cell-type  
96 prediction of chromatin states by multi-task learning based on genome-wide pre-training on  
97 epigenomic data (**Fig. 1 and Fig. S6**). EpiGePT is composed of four modules, including a  
98 sequence module, a TF module, a transformer module, and a prediction module. The sequence  
99 module is responsible for processing the long DNA sequence of interest (e.g., 128 kb) by  
100 employing a series of convolutional and pooling blocks (e.g., 5) to extract a comprehensive set  
101 of sequence features. By reducing the input length by  $2^5=128$  times through pooling operations,  
102 this module effectively compresses the input information while retaining essential features. The  
103 TF module is specifically designed to extract cell-type-specific features by taking the  
104 expression of transcription factors in the given context, as well as their corresponding motif  
105 score into account. This module helps capture the unique characteristics of each cell type by  
106 considering the binding status of TFs involved in gene regulation. In the transformer module,  
107 each token corresponds to a genomic bin in the original DNA sequence and has hybrid features  
108 derived from both sequence and TFs. The module leverages self-attention mechanisms to learn  
109 the comprehensive relationships among the input bins, enabling the model to make predictions  
110 of multiple chromatin states under the given context cellular. By taking advantage of this  
111 approach, EpiGePT provides a powerful tool for predicting multiple chromatin states and  
112 enables researchers to gain insights into the underlying regulatory mechanisms of the genome.

## 113 **EpiGePT enables genome-wide prediction of chromatin states**

114 To assess the predictive performance for epigenomic signals of EpiGePT, specifically in  
115 predicting chromatin accessibility, a comprehensive evaluation was conducted. We first applied  
116 EpiGePT to predict the chromatin accessibility based on the widely available public DNase-  
117 seq<sup>14</sup> data across diverse cell types or tissues. In brief, DNase-seq data across 129 cell types  
118 were collected from the ENCODE<sup>12</sup> project. After data preprocessing and normalization (see  
119 Methods), 1,175,374 genomic regions were extracted where each pair of cell type and genomic  
120 regions constitutes a training instance. We meticulously devised comprehensive experimental  
121 settings by partitioning the training and test sets based on either genomic regions or cell types.  
122 In detail, we employed the following three data partitioning settings for a comprehensive  
123 evaluation (Fig. S1, Text S1). For “cross-cell-type” prediction, we partitioned the data into  
124 training and testing sets based on cell types. For “cross-region” prediction, we partitioned the  
125 data into training and testing sets based on the genomic regions. For “cross-both” prediction,  
126 we conducted rigorous data split to ensure that both the cell types and genomic regions in the  
127 test stage are unseen during the training process. We employed three evaluation metrics, namely  
128 Pearson correlation coefficient, Spearman correlation coefficient and prediction square error,  
129 to assess the similarity between the predicted and true values of DNase signals (See Methods).  
130 It is shown that EpiGePT consistently outperforms other competing methods, including  
131 Enformer<sup>11</sup>, BIRD<sup>15</sup>, and ChromDragoNN<sup>16</sup> by a relatively large margin under the above  
132 experimental settings (**Fig. 2A** and Fig. S2). EpiGePT achieves 5.0%, 8.9%, and 5.2 % higher  
133 performance than Enformer, the best baseline method, in terms of the mean Pearson correlation  
134 coefficient under three data-partition settings, respectively (**Fig. 2B**). Besides the chromatin

135 accessibility regression task, we also designed binary chromatin accessibility status prediction  
136 task by assessing whether a peak exists within the corresponding genomic bin (>50% overlap).  
137 We made slight adjustments to the regression model by modifying the activation function and  
138 loss function to accommodate the binary classification task (See methods). The results show  
139 that EpiGePT achieves an average auPRC (area under the precision-recall curve) of 0.767  
140 compared to 0.727 of Enformer<sup>11</sup>, 0.623 of DeepCAGE<sup>17</sup> and 0.476 of ChromDragoNN<sup>16</sup> (**Fig.**  
141 **2C**).

142 Next, we extended the chromatin state prediction task from a single target to multiple targets  
143 by predicting multiple chromatin states, including chromatin accessibility, CTCF<sup>18</sup>, ChIP-seq,  
144 and six types of different histone modifications<sup>19</sup> (See Methods). When considering eight  
145 different chromatin states, only 28 cell types have the corresponding available data  
146 simultaneously. After preprocessing, 13,300 genomic regions each with a length of 128 kbp  
147 were extracted, which cover 56.7% of the whole genome. However, compared to the data in  
148 the DNase-only prediction experiment, the correlation coefficient was reduced due to the  
149 prevalence of a substantial number of zero signals in the genomic regions being predicted.  
150 Using a similar data split strategy as the single target for cross-cell-type prediction, EpiGePT  
151 demonstrated a mean Pearson correlation coefficient between 0.259 to 0.566 of different  
152 chromatin states in the test cell types (**Fig. 2D**). Specifically, EpiGePT achieves remarkably  
153 high performance in predicting chromatin state signals for certain cell types, such as the colon  
154 tissue, with a Pearson correlation coefficient of 0.888. Furthermore, as it shown in Fig. S3C, it  
155 significantly outperformed Enformer in terms of performance across these tested cell types and  
156 different signals (one-side  $p$ -value < 2.79e-10 under binomial hypothesis test). To make the



157 chromatin states prediction task more illustrative, several tracks of predicted chromatin states  
158 and the corresponding ground truth chromatin states were displayed. For instance, at the  
159 position of from 61,056,000 to 61,184,000 on chromosome 20, we used the UCSC genome  
160 browser<sup>20</sup> to show the predicted values and true values of CTCF (Pearson correlation coefficient  
161 of 0.518) and DNase signals (Pearson correlation coefficient of 0.869), as well as the regulatory  
162 relationships within this region. (Fig. S2A). In addition, we also compared EpiGePT with  
163 ChromDragoNN<sup>16</sup> on binary and quaternary classification tasks based on ChromHMM<sup>21</sup>  
164 annotations (Fig. S3). EpiGePT achieved an average auROC (area under the receiver operating  
165 characteristic curve) of 0.855 in binary classification, significantly higher than that of  
166 ChromDragoNN<sup>16</sup> (0.774). In quaternary classification, EpiGePT achieved a macro-auROC of  
167 0.879, also significantly higher than ChromDragoNN<sup>16</sup> (0.856, one-side  $p$ -value < 0.001).  
168 These results demonstrate the effectiveness and accuracy of EpiGePT in predicting multiple  
169 chromatin states, leveraging the four modules. The effectiveness and prediction power achieved,  
170 in conjunction with the self-attention mechanism, lays the foundation for deciphering  
171 regulatory relationships.

172 To further verify the roles of the main modules in the model, we conducted the ablation  
173 experiments on the model architecture. For TF module ablation, the above experimental results  
174 compared to EpiGePT without TF module (EpiGePT-seq) and EpiGePT have demonstrated that  
175 EpiGePT outperforms EpiGePT-seq in cross-cell-type prediction of DNase signals, with an  
176 average Pearson correlation coefficient of 0.714 and a median of 0.74 for EpiGePT-seq, while  
177 EpiGePT achieves 0.756 (average) and 0.787 (median). In addition, the inclusion of the TF  
178 module enables EpiGePT to predict chromatin states at the locus level for different cell types.

179 However, like Enformer, EpiGePT-seq predicts the same values for different cell types at the  
180 same locus, resulting in a zero correlation for cross-cell-type prediction. We examined the  
181 impact of the TF module on multi-task prediction by employing three methods, namely  
182 replacing TF scores with zero, adding random noise to TF, and removing motif binding scores.  
183 The results indicated that when the expression of TFs was set to zero, the prediction of H3K27ac  
184 yielded a Pearson correlation coefficient of 0.190. However, incorporating the TF module  
185 significantly improved the coefficient to 0.543, demonstrating a beneficial impact of the TF  
186 module.

187 For sequence module ablation, we randomly subsampled 10,000 genomic bins and 20 cell  
188 types to train a TF-only model. The results indicated that removing the sequence  
189 module resulted in an average decrease of 0.084 in the Pearson correlation coefficients  
190 of the eight signals on a cell-type wise basis, and with a particularly significant decrease  
191 of 0.13 in predicting H3K4me3 signals (Fig. S4A).

192 For multi-task module, we predicted the eight chromatin states involved in training  
193 using eight individual models for single-task prediction. The results were evaluated on  
194 a cross-cell type prediction manner. In the case of predicting the signal of H3K4me1,  
195 the average Pearson correlation decreased from 0.408 to 0.329. When predicting the  
196 H3K4me1 signal, the average Pearson correlation coefficient decreased from 0.408 to  
197 0.329. Similarly, the overall prediction performance for the eight signals declined by  
198 0.074 (**Fig. 4B**). This decrease may be attributed to the intricate nature of gene  
199 regulation. The distinct chromatin states can complement and synergize with each other  
200 through multi-task learning, allowing the model to gain deeper biological insights

201 compared to a single-target prediction model.

202 Furthermore, we performed additional experiments to investigate the effect of the  
203 number of cell lines on the prediction performance. Specifically, we focused on DNase  
204 predictions and randomly downsampled the training cell types from 103 to 75, 50, 25  
205 for each of the five folds in the cross-validation experiment. The results demonstrated  
206 a strong positive correlation between the number of cell lines and the prediction  
207 performance. Under five-fold cross-validation, the median Pearson correlation  
208 coefficient on the test set across 129 cell types decreased from 0.793 to 0.790, 0.761,  
209 and 0.732, respectively. These findings suggest that our current model has potential  
210 room for improvement and additional training with more cell lines will lead to even  
211 better predictive performance, thereby offering more comprehensive insights into the  
212 regulatory mechanisms for researchers (Fig. S4C). In summary, EpiGePT demonstrated  
213 superior performance in predicting both single and multiple epigenomic signals over  
214 existing methods, providing a robust foundation for decoding the complex landscape  
215 of gene regulation.

### 216 **EpiGePT facilitates long-range chromatin interaction identification**

217 We examined the capacity of EpiGePT for predicting long-range chromatin interactions, which  
218 play a critical role in preserving chromatin architecture and elucidating 3D contacts between  
219 distal regulatory elements and target genes. Traditional methods typically take short DNA  
220 sequence (e.g., 1kbp) as input, thus cannot take the long-range chromatin interactions into  
221 consideration. During the training of EpiGePT model, the self-attention mechanism in the

222 transformer module plays an important role in capturing the potential interactions between  
223 different DNA bins. We utilized the cell-type specific self-attention scores to predict chromatin  
224 interactions, including enhancer-promoter and silencer-promoter interactions (see Methods).  
225 We initially investigated whether EpiGePT can differentiate experimentally validated enhancer-  
226 promoter interactions from other interactions. Two datasets containing 664 and 5,091 candidate  
227 enhancer-promoter interactions or element-TSS interactions obtained by CRISPRi<sup>22</sup>  
228 experiments were used and further filtered and stratified by the distance. In the Gasperini et  
229 al<sup>23</sup>. dataset, EpiGePT consistently outperform EpiGePT-seq and Enformer by achieving the  
230 highest auPRC in all groups. For instance, EpiGePT achieved auPRC of 0.949, 0.726, and 0.810  
231 for identifying enhancer-promoter pairs in the 0-3 kbp, 3-20 kbp, and 20-64 kbp ranges,  
232 respectively (**Fig. 3A and Fig. S8**). In the Fulco et al.<sup>24</sup> dataset, EpiGePT obtains better  
233 performance than EpiGePT-seq in most groups, which illustrates the positive benefit of the cell-  
234 type-specificity brought in the TF module. EpiGePT consistently outperforms Enformer across  
235 different groups by a relatively large margin. As shown in Fig. 3A, EpiGePT achieves an auPRC  
236 of 0.618, compared to 0.531 of Enformer, and 0.568 of EpiGePT-seq in 0-12kbp group.

237 Next, we explored whether EpiGePT is also capable of predicting the promoter-silencer  
238 interactions. Since there is very limited experiment-validated silencer-promoter interactions,  
239 we downloaded putative silencers from the SilencerDB<sup>25</sup> and used the promoter of annotated  
240 nearest gene as the potential target. For negative silencer-promoter pairs, we selected the same  
241 promoter and equidistant genomic regions in the opposite direction to ensure the consistency  
242 of distance distributions between positive and negative sample pairs at different distance levels.  
243 As a result, EpiGePT achieves a better performance in discerning positive silencer-promoter

244 pairs from negative pairs than Enformer by a relatively large margin. For instance, EpiGePT  
245 displays an auROC of 0.575 in long-range interactions (32-64kbp) with positive-to-negative  
246 ratio 1:1 setting, compared to 0.547 of EpiGePT-seq, and 0.483 of Enformer (**Fig. 3B**).

247 According to these results, the self-attention mechanism significantly enhances the ability to  
248 identify potential chromatin interactions and increases the interpretability of the model.

249 The HiChIP<sup>26</sup> sequencing technology provides unprecedented opportunities to uncover 3D  
250 genomic interactions. We aim to investigate the predictive performance of EpiGePT on 3D  
251 genome interaction based on HiChIP data. Here, we employ the same strategy as described  
252 above to calculate attention scores for the regulatory element-promoter pairs and collected  
253 HiChIP loops on K562 and GM12878 cell lines from the HiChIPdb<sup>27</sup>. The results demonstrate  
254 that incorporating TF expression data into EpiGePT leads to enhanced predictive performance  
255 for HiChIP loops compared to the pure sequence models Enformer and EpiGePT-seq, across  
256 diverse distance ranges and in two distinct cell lines. Specifically, within the 20-40 kbp distance  
257 range on K562 cell line, EpiGePT achieves an auROC of 0.599 for the 1:1 positive-to-negative  
258 ratio, surpassing Enformer's performance of 0.545 (**Fig. 3E**). These findings suggest that, even  
259 without any fine-tuning, EpiGePT's attention scores encompass more accurate and  
260 comprehensive biological information, underscoring its potential for capturing intricate  
261 genomic interactions.

262 To better understand the self-attention mechanism of EpiGePT and bridge the gap between the  
263 model and its interpretability, we visualized the attention matrices after normalization (**Fig. 3C**).

264 The visualization shows prominent scores between certain genomic bins, indicating the  
265 potential presence of interactions. We centered on the transcription start site (TSS) of the CHD4

266 gene and calculated the self-attention scores between the genomic bins within its upstream and  
267 downstream 128kbp. The attention scores exhibited peaks near the regulatory elements in the  
268 vicinity of the TSS, which further validates the feasibility and accuracy of our prediction of  
269 enhancer-promoter interactions (**Fig. 3D**).

## 270 **EpiGePT improves variant effect prediction**

271 One of the most essential tasks for EpiGePT is to dissect the effect of genetic variants that occur  
272 in different genomic regions. As most of the variants identified by the GWAS studies lie in the  
273 non-coding regions of the genome, which makes it difficult to interpret the variant effect, most  
274 sequence-based computational models directly take the alleles sequence as input and compare  
275 the difference in the predicted regulatory activity. The advantage of EpiGePT model comes  
276 from the TF module where variant effect can be estimated under any given cellular context.  
277 This is extremely helpful when predicting the effect of the disease- or phenotype-associated  
278 SNPs. To test the ability of EpiGePT in variant effect prediction, we first collected an eQTLs  
279 dataset<sup>28</sup> that contains 20,913 causal and non-causal variant-gene pairs in total across 49  
280 different tissues from the supplementary data of Wang et al<sup>28</sup>. EpiGePT and EpiGePT-seq are  
281 then applied to estimate the log-odds scores (LOS) given both the reference and alternative DNA  
282 sequence and the corresponding relevant TF profile (see Methods, **Fig. 4A**). Finally, a random  
283 forest classifier is trained based on the LOS scores across different chromatin states. The  
284 experimental results show that in the lung tissue, EpiGePT demonstrates an auPRC of 0.922,  
285 compared to 0.873 of Enformer in distinguishing causal SNPs. To verify the effectiveness of  
286 TF module, we replace the TF profile of lung with stomach, which is much less relevant to the  
287 lung tissue. The auPRC decreases from 0.922 to 0.892 (**Fig. 4B**). Similarly, EpiGePT-seq can

288 achieve an average auPRC of 0.910, compared to 0.898 of Enformer using 5-fold cross-  
289 validation for predicting causal variants on 48 extracted tissues (Fig. S3D). In the adrenal gland  
290 tissue, EpiGePT-seq demonstrates an average auPRC of 0.883, compared to only 0.842 of  
291 Enformer. The above experiments show the predictive power of EpiGePT in estimating the  
292 variant effect.

293 To further evaluate the performance of EpiGePT in predicting disease-associated variants, we  
294 extracted 52, 876 pathogenic SNPs from the ClinVar<sup>29</sup> database and 418, 863 benign SNPs from  
295 the ClinVar database, also with 84, 095 benign SNPs from the ExAC database<sup>30</sup> as positive and  
296 negative sets, respectively. We defined a 64kbp region surrounding each pathogenic SNP as the  
297 risk region. We screened all benign and likely benign SNPs that fall within the risk region from  
298 the negative sets for classification. As the relevant tissue or cell type information is not available,  
299 we concatenated the LOS of the eight epigenomic signals and self-attention scores across 28  
300 cell types into a single 252-dimensional vector and then train a classifier for predicting whether  
301 the given SNP is pathogenic (see Methods). To assess the whether the 252-dimensional features  
302 are beneficial in predicting pathogenic SNPs, we concatenated it with 52 annotations from  
303 CADD<sup>31</sup>, resulting in a comprehensive feature vector. Subsequently, we compared the  
304 performance of this combined feature vector with that of the individual features derived  
305 exclusively from CADD. We then utilized these two sets of features to train multi-layer  
306 perceptron (MLP) classifiers separately. The results demonstrate that incorporating EpiGePT's  
307 variant effect features from multiple cell types significantly enhances the performance of the  
308 classifier in predicting pathogenic SNPs. Specifically, when the positive-to-negative sample  
309 ratio was set to 1:1, the average auROC increased from 0.772 to 0.806, and the average accuracy

310 increased from 0.690 to 0.723 (**Fig. 4C**). This observation indicates that features extracted by  
311 EpiGePT provide a valuable complement to CADD annotation, enabling a more comprehensive  
312 depiction of variant characteristics, and thereby facilitating the discovery of disease-associated  
313 variants.

#### 314 **EpiGePT prioritizes potential SNPs associated with comorbidities of COVID-19**

315 We investigated whether the ability of EpiGePT to predict variant effects could help in the  
316 discovery of key SNPs related to COVID-19. COVID-19 is an infectious disease caused by the  
317 SARS-CoV-2 virus, which emerged in late 2019 and quickly spread around the world, causing  
318 a global pandemic<sup>32</sup>. In order to validate the ability of EpiGePT in identifying key SNPs, we  
319 collected GWAS data from the COVID-19 host genetics<sup>33</sup>, including 9,484 variants. These  
320 variants were derived from 4,933 patients with confirmed severe respiratory symptoms and  
321 1,398,672 control individuals without COVID-19 symptoms. To validate the ability of the  
322 model to identify COVID-19-related SNPs, we firstly defined a risk region around the selected  
323 COVID-19-related SNPs and computed the rank of the variant score of pathogenic SNPs within  
324 the surrounding benign SNPs from the ClinVar database. The expected rank for random  
325 guessing (uniform distribution) is 0.5. Interestingly, we found that the average rank of COVID-  
326 19-related SNPs was significantly lower than 0.5 across several tissues or cell types (**Fig. 4D**).  
327 For instance, when lung expression data was employed and a 6-kbp risk region was examined,  
328 the median rank was 0.250, and when expression data of esophagus squamous epithelium was  
329 used the median rank was 0.333, significantly lower than 0.5 (one-side *p*-value of 0.013 under  
330 one-sided Binomial Test). However, when we employed the expression data from smooth  
331 muscle cells, which are a more widespread cell type with lower relevance to COVID-19, the



332 median rank exhibited a notable decrease to 0.381. Notably, when focusing on the 40-kbp risk  
333 region, the median rank further declined to 0.850, higher than 0.5. These findings suggest that  
334 EpiGePT model is able to prioritize the COVID-19-related SNPs thus shedding lights on  
335 finding the potential disease-associated variants with our pretrained large language model.

336 Next, based on the aforementioned findings, we aimed to use EpiGePT to identify genes that  
337 are highly related to COVID-19. Since the genetic pathology of COVID-19 is not yet clear and  
338 the earliest lesion is in the lungs, we ranked all 9,484 possible SNPs using lung expression data.  
339 We then identified the SNPs with the highest ranks and performed gene ontology enrichment  
340 analysis on nearest genes of the 100 top ranked SNPs (**Fig. 4E**). The enrichment results revealed  
341 potential biological processes that are relevant to COVID-19, such as the regulation of  
342 glucokinase activity which is associated with the homeostasis of human blood glucose<sup>34</sup>.  
343 Notably, diabetes mellitus, a condition closely associated with hyperglycemia, is a typical  
344 comorbidity of COVID-19<sup>35</sup>. Besides, among the top 10 potential genes that scored the highest,  
345 we identified that the TBC1D4 gene, which regulates glucose homeostasis, is potentially  
346 associated with COVID-19 comorbidities. Our findings are consistent with previous research  
347 by Pellegrina et al.<sup>36</sup> and highlights the potential of our EpiGePT approach in discovering new  
348 genetic markers that may be implicated in the pathogenesis of COVID-19. Overall, our  
349 EpiGePT model provides new perspectives for understanding how the genetic variants could  
350 contribute to the COVID-19 susceptibility and severity.

### 351 **Fine-tuning on EpiGePT enables accurate prediction of regulatory interactions**

352 Fine-tuning is an strategy that transfers the knowledge of a pretrained model to new tasks,

353 which is particularly prevalent in language models such as GPT<sup>37</sup> and BERT<sup>38</sup>. Here, we  
354 finetuned a pretrained EpiGePT model on a new task for predicting the 3D genome interaction.  
355 Given the HiChIP H3K27ac data from K562 and GM12878 cell lines, the features of two  
356 anchors were extracted from a pretrained EpiGePT model and then fed to a finetune network  
357 to predict whether it is a HiChIP loop. We compared EpiGePT with pretrain and finetuning  
358 strategy to two baselines, DeepTACT<sup>39</sup> and a k-mer frequency<sup>40</sup> based method (see Methods).  
359 The results illustrate that EpiGePT exhibits a superior classification performance across diverse  
360 distance ranges compared to baselines. For example, in the GM12878 cell line within the 20-  
361 40kbp distance range, EpiGePT demonstrates a significantly improved predictive performance  
362 with an auROC of 0.949, surpassing 0.866 of DeepTACT<sup>39</sup> and 0.771 of Kmer (**Fig. 4F** and  
363 **Fig. S7**). This significant improvement achieved through fine-tuning EpiGePT on a limited  
364 dataset aligns well with the concept of few-shot learners<sup>1</sup>, highlighting the power of the  
365 pretrained EpiGePT model.

### 366 **EpiGePT encompasses the regulatory relationships between TFs and target genes.**

367 One of the key differentiating factors of EpiGePT compared to other sequence models lies in  
368 its integration of TF binding status and TF expression. This unique feature empowers EpiGePT  
369 to capture potential regulatory relationships embedded within the genomic sequence. In this  
370 study, we specifically aimed to validate whether EpiGePT learns the regulatory relationships  
371 between TFs and target genes (TGs). We defined gradient importance scores (GIS) based on  
372 the absolute gradient values of predicted epigenomic signals w.r.t. TF profile to rank TFs give  
373 a TG (see Methods). Particularly, we collected 15 TFs that play critical regulatory roles in  
374 embryonic stem cells (ESC)<sup>41, 42</sup> and validated their interaction relationships using computed

375 GIS. As an example, for a target gene STAT3 that plays essential role for ESC pluripotency<sup>43</sup>,  
376 we computed GIS for each core TF across 1000 genomic bins and find other key TFs in ESC  
377 ranked 1<sup>st</sup> (REST) and 2<sup>nd</sup> (POU5F1) at specific bins (**Fig. 5A-B**). Interestingly, the GO terms  
378 enriched by the top 10% prioritized TF coding genes also included biological processes of  
379 embryonic cell differentiation and development when we focus on the genomic bin that  
380 POU5F1 ranked 2<sup>nd</sup> (**Fig. 5C**). We selected a TF as the target gene and calculated the integrated  
381 GIS (IGIS) score for another key TF across eight epigenomic signals. Multiple TF-gene pairs  
382 identified by IGIS that showed significant associations with POU5F1, such as ESRRB-  
383 POU5F1<sup>44</sup> (rank 2<sup>nd</sup>), and ETV5-POU5F1<sup>45</sup> (rank 5<sup>th</sup>). Furthermore, we use TF-TG  
384 relationships from either ChIP-seq data or external databases as ground truth to validate  
385 whether IGIS is effective in prioritizing the TFs given a TG. First, we defined potential TF-  
386 target gene pairs based on TF ChIP-seq data specific to certain cell types among all human  
387 genes (see Methods). The results demonstrated a significant difference in rank between TF-  
388 target gene pairs and TF-non-target gene pairs based on the IGIS score (**Fig. 5D**), with the  
389 former exhibiting considerably higher ranks (one-side  $p$ -value  $< 0.001$ ). Second, we collected  
390 TF-target regulatory network data from two publicly available databases. We obtained a total  
391 of 1,066 TF-gene pairs from the GRNdb<sup>46</sup> database based on liver-specific GTEx data, and  
392 2,705 TF-gene pairs from the TRRUST<sup>47</sup> database after filtering. Then we calculated the rank  
393 of each TF based on GIS of the TF expression and a genomic bin-level mask for each pair.  
394 Interestingly, when using liver expression data, we found that the average rank of TFs from  
395 TRRUST was 7.9%, significantly lower than the rank based on expression values (one-side  $p$ -  
396 value  $< 1e-5$ ). Similarly, based on the GRNdb data, the majority of TF-gene pairs obtained had

397 TF ranks within the range of 20%, and the mean of this distribution was significantly lower  
398 than the rank based on expression values with one-side  $p$ -value  $< 1e-5$  (**Fig. 5E**). For instance,  
399 TMEM55B plays a significant role in regulating lysosome movement, and is regulated by sterol  
400 response element binding factor 2 (SREBF2)<sup>48</sup>, while GIS enable the identification of SREBF2  
401 as the top-ranked TF associated with TMEM55B, further validating the role of GIS in  
402 prioritizing functional TFs. The comprehensive validation from both ChIP-seq datasets and  
403 external databases further support the effectiveness of GIS in identifying context-specific TF-  
404 TG relationships.

#### 405 **Online prediction tool for EpiGePT**

406 In order to facilitate the utilization of EpiGePT for the prediction of multiple chromatin  
407 states of any cellular context and any genomic regions, especially for research  
408 personnel who lack coding expertise, we have developed a user-friendly online web  
409 server, named EpiGePT-online (<https://health.tsinghua.edu.cn/epigept/>) (Text S2). The  
410 online web server was developed using PHP, JavaScript and HTML, which provides an  
411 interactive web interface for online prediction of 8 chromatin states of specific genomic regions  
412 (**Fig. 6**). Users can obtain the predicted signals of multiple genomic regions by submitting a  
413 region file and a TF expression file of 711 selected TFs (Supplementary Table S3), or obtain  
414 predicted signals of specific regions directly by selecting genomic locus. As to the two types of  
415 input files, we provide example files to demonstrate their formats, and accept expression files  
416 stored in either numpy or csv formats, to increase the universality of the web server (Fig. S5).  
417 The web server outputs the results in a web summary html, which saves significant amount of  
418 time for installation and implementation. Furthermore, we provide a detailed tutorial to enable

419 users to quickly learn how to use our website. We anticipate that this web server will assist  
420 researchers in predicting chromatin states of specific cell types and further deepening  
421 their understanding of gene regulatory mechanisms.

## 422 **Discussion**

423 In this paper, we introduced EpiGePT, a transformer-based large language model, for predicting  
424 the chromatin states given any cellular context. Compared with the existing machine learning  
425 based computational methods, EpiGePT takes transcription factor profile and DNA sequence  
426 information as inputs by multitask learning and self-attention mechanism within a unified  
427 model. With these two types of input information and four modules of network architecture,  
428 EpiGePT overcomes the limitation of the existing models and demonstrates state-of-art  
429 performance in prediction of multiple chromatin signals in diverse experimental settings. With  
430 the superior predictive performance of EpiGePT, we are able to investigate one of the  
431 fundamental questions in functional genomics: how transcription factors and cis-regulatory  
432 elements regulate gene activity. In this work, we investigated this question from two aspects:  
433 1) identifying the interactions of cis-regulatory elements and their target genes with the help of  
434 self-attention mechanism in EpiGePT; 2) estimating the variant effect based on the LOS scores  
435 computed by the outputs of EpiGePT to assist in discovering human disease-associated SNPs.  
436 First, the self-attention scores between tokens can provides us with an intuitive and quantitative  
437 measure of the interaction level between different genomic regions, which offers new  
438 opportunity to discover the target gene of cis-regulatory elements and find the interpretability  
439 of EpiGePT. Second, the LOS scores of the multiple chromatin signals from different tissue or  
440 cell lines are complementing each other, which provides us with a more comprehensive

441 characterization of the variant and enables accurate prediction of the variant impact. Such  
442 variant effect prediction by EpiGePT establishes a foundation for understanding the underlying  
443 relationship between genetic variations and disease mechanisms.

444 There exist several extensions and refinements that can be applied to further improve the  
445 EpiGePT model. Firstly, the incorporation of chromatin regulators (CRs) as trans-acting factors  
446 into the TF module could enhance the modeling of regulated transcription processes, thereby  
447 increasing the accuracy of the predictions. Secondly, the inclusion of high-order interactions  
448 between TFs in the framework could provide a more comprehensive representation of the  
449 regulatory relationships, and potentially enhance the predictive performance. Third, the  
450 application of EpiGePT to single-cell genomics could enable the profiling of chromatin signals  
451 at single-cell resolution, facilitating a holistic understanding of regulatory heterogeneity in  
452 different cell subpopulations for researchers.

453 Based on EpiGePT, users are able to predict multiple chromatin profiles in different cell lines  
454 or tissues, which could provide a foundation for biological discovery, decoding transcriptional  
455 regulation mechanisms, and investigating disease mechanisms. We anticipate that EpiGePT can  
456 provide valuable insights to researchers in understanding regulatory mechanisms.

## 457 **Methods**

### 458 **Data processing**

459 **Chromatin accessibility data and Expression data** We used three different datasets in the  
460 experiments. For chromatin accessible data, we downloaded DNase bam files and narrow peaks  
461 across 129 human biosamples from ENCODE<sup>12</sup> project (Supplementary table S1 and S2). We  
462 divided the human hg19 genome into 200bp non-overlapping locus (use bin instead), and we  
463 assigned the label for each locus in each cell type. For the regression design, we pooled the bam  
464 files of multiple replicates for a cell type (Supplementary table S1 and S2), and obtain the raw  
465 read count  $n_{lk}$  for locus  $l$  in cell type  $k$ . We normalized the raw read count in order to eliminate  
466 the effect of sequencing depths, in the form of  $\tilde{n}_{lk} = Nn_{lk}/N_k$ , where  $N_k$  denotes the total  
467 number of pooled reads for cell type  $k$  and  $N = \min_k N_k$  denotes the minimal number of pooled  
468 reads across all cell types. The normalized read counts are further log transformed with pseudo  
469 count 1, which represent the continuous level of chromatin accessibility. For binary  
470 classification design, we assigned a binary label  $y_{lk}$  to 1 if the number of raw read counts of  
471 the locus  $l$  in the cell type  $k$  greater than 30, which represent the locus is an accessible region  
472 in this cell type, resulting in the identification of regions as accessible in 13% on average and  
473 8% at median in the screened genomic regions across 129 cell types. The proportion of open  
474 regions varies among different cell types, and the average openness level mentioned above is  
475 generally consistent with that maintained in ChromDragoNN<sup>16</sup>.

476 RNA-seq data of the 711 human transcription factors were downloaded and extracted from the  
477 ENCODE project (Supplementary table S5 and S6). We perform log transformation with

478 pseudo count 1 and quantile normalization based on TPM values. The normalized TPM values  
479 were averaged across replicates and mean expression profile of each cell type was finally used  
480 to calculated of the transcription feature.

481 **Multiple chromatin signals data** DNase-seq, RNA-seq and ChIP-seq data were also  
482 downloaded from ENCODE project (Supplementary table S3, S4 and S6). We applied the same  
483 process to these data as above, and finally we obtained the 8 chromatin signals of 13,300,000  
484 bins of 128bp in 28 cell types. The continuous level of chromatin signals we extracted were  
485 'DNase', 'CTCF', 'H3K27ac', 'H3K4me3', 'H3K36me3', 'H3K27me3', 'H3K9me3' and  
486 'H3K4me1', which includes crucial epigenetic modifications and markers for gene regulation  
487 and transcription.

488 **Chromatin states data** We downloaded the 15-state ChromHMM<sup>21</sup> annotations across 127  
489 epigenomes from the ROADMAP project. The state of chromatin is annotated for each 200bp  
490 bin in a specific cell type. RNA-seq data across 56 cell types of TFs was download and extracted  
491 from the ROADMAP<sup>49</sup> project (Supplementary table S7 and S8). Subsequently, we mapped  
492 these 711 transcription factors to the downloaded RNA-seq data, resulting in the identification  
493 of RNA-seq data for 642 transcription factors. In the subsequent experiments, we utilized the  
494 expression data of these 642 transcription factors. We finally calculated the normalized TPM  
495 values of the 642 TFs on 56 cell types we extracted for the using in the classification model.  
496 For coarse grain chromatin state prediction, we took the state 'Quies' as low signal regions and  
497 other states as signal regions. For fine grain chromatin state prediction, we extracted the state  
498 'TssA', 'TssAFInk', 'TssBiv' and 'BivFInk' as TSS regions, state 'EnhG', 'Enh' and 'EnhBiv' as  
499 enhancer regions, 'Quies' as low signal regions and other state as other regions. To balance the



500 number of different chromatin states, we downsampled the low signal regions and obtained  
501 921,074 locus each cell line finally.

## 502 **Model architecture**

### 503 **Sequence module and Transformer module**

504 As shown in Figure 1 and Fig. S6A, the sequence module receives a one-hot matrix ( $A =$   
505  $[0,0,0,1]$ ,  $C = [0,1,0,0]$ ,  $G = [0,0,1,0]$ ,  $T = [0,0,0,1]$ ) of size  $(128000,4)$  as input, representing a  
506 sequence of 128 kilobase pairs (kbps) and contains five 1-dimensional convolutional blocks to  
507 extract DNA sequence features. Each block includes a convolutional layer and a maxpooling  
508 layer (Fig. S6B). The first convolutional layer considers the input channels as 4 and performs  
509 convolution along the sequence direction. The input sequence features are one-hot embeddings  
510 of size  $L \times 4$ , where  $L$  denotes the length of the input long range DNA sequence. After 5  
511 maxpooling layers, the output size of sequence feature is  $L/N \times C$ , where  $C$  denotes the hyper-  
512 parameter for sequence embedding and  $N$  denotes the length of locus to predict. We set  $C$  to  
513 256 in the pre-training stage of chromatin accessibility prediction experiments. Rectified linear  
514 units (ReLU) are used after each convolution operation for keeping positive activations and  
515 setting negative activation values to zeros. Sequence features were then concatenated with  
516 transcriptomics features, and we finally obtained a vector of size  $L/N \times (C + n_{TF})$ , where  $n_{TF}$   
517 denotes the dimension of the transcription factors features after padding. In our model, after  
518 adding padding to the 711 TFs, the  $n_{TF}$  is set to 712. Therefore, the input token number for the  
519 transformer module is 1000, and each token embedding has a dimensionality of 968.

520 We utilize the transformer module to integrate information from both the sequence and

521 transcription factors (TFs), enabling the capturing of long-range interactions between genomic  
522 bins. We applied  $N_t$  layers of Transformer encoder with  $n_{head}$  different attention heads to the  
523 token embedding sequence. The input  $X$  of the transformer encoder is a genomic bin sequence  
524 with dimensions (*Sequence length, embedding dim*). Specifically, this dimension is (1000,  
525 968) in EpiGePT, indicating that input genomic bin sequence has a length of 1000, and each  
526 genomic bin has an embedded representation that combines the sequence information with cell-  
527 type-specific features with dimension of 968. Each Transformer encoder includes a multi-head  
528 self-attention mechanism and a feed-forward neural network. For self-attention in each head,  
529 the calculation is based on the matrix operation.

$$530 \quad \text{Attention}(Q, K, V) = \text{softmax}\left(\frac{QK^T}{d_k}\right)V$$

531 For multi-head attention, Transformer encoder learns parameter matrices  $W_i^Q \in$   
532  $\mathbb{R}^{d_{model} \times d_Q}$ ,  $W_i^K \in \mathbb{R}^{d_{model} \times d_K}$  and  $W_i^V \in \mathbb{R}^{d_{model} \times d_V}$  for the  $i_{th}$  head and concatenate the  
533 multiple heads to do the projection.

$$534 \quad Q_i = X \times W_i^Q, K_i = X \times W_i^K, V_i = X \times W_i^V$$

535 Where  $d_{model}$  denotes the dimension of token in the input sequence  $X$ , which is 968 in  
536 EpiGePT and  $d_Q = d_K = d_V = 512$ . The matrices  $Q$ ,  $K$ , and  $V$  are obtained by the application  
537 of mapping functions represented by  $W_i^Q$ ,  $W_i^K$  and  $W_i^V$ , followed by concatenating of  $Q_i$  to  $Q$ ,  
538  $K_i$  to  $K$ , and  $V$  to  $V$ . These mapping functions serve to transform the concatenated embeddings  
539 into the resulting matrices. We set  $N_t$  to 16 for the chromatin accessible prediction experiments,  
540  $N_t$  to 12 for the chromatin state classification and multiple chromatin signals prediction  
541 experiments, and set  $n_{head}$  to 8 for all experiments.

542 The regression model, the output layer uses a linear transformation and use mean square error  
543 (MSE) as the loss function. For classification model, the output layer uses a linear  
544 transformation combined with a sigmoid function, and use the cross-entropy loss for  
545 classification experiments.

## 546 **TF module**

547 For binding status, we scanned the input bins for potential binding sites for a set of 711 human  
548 transcription factors from HOCOMOCO database<sup>50</sup> with the tool Homer<sup>51</sup> (Table S5). We then  
549 selected the maximum score of reported binding status for each transcription factor to obtain a  
550 vector of 711 dimensions as the motif feature for each DNA bin. For gene expression, we  
551 focused on log-transformed TPM values of the 711 transcription factors and obtained a vector  
552 of 711 dimensions after quantile normalization as the expression feature. With these data, we  
553 combined the two vectors of motif and expression features by taking the element-wise product,  
554 and we concatenated the result to the output of sequence module.

## 555 **Model evaluation**

556 To evaluate our model, we applied five-fold cross-validation in the different experiments on  
557 cell-type level. For chromatin accessible experiments, the 129 cell lines are partitioned into a  
558 training set and a testing set randomly.

559 Cell-type-wise metrics are defined to evaluate our method in different experiments, which were  
560 calculate with the data within a test cell type across all genomic locus. For binary classification  
561 design, we used cell-type-wise auPRC and auROC to evaluate our EpiGePT. Let  $Y_{L \times K}$  and  $\hat{Y}_{L \times K}$   
562 be the true and predicted matrix, where L denotes the number of locus and K denotes the number

563 of test cell types. We calculated the auPRC and auROC for each  $(y_{1i}, y_{2i}, \dots, y_{Li})$  and  
564  $(\hat{y}_{1i}, \hat{y}_{2i}, \dots, \hat{y}_{Li})$ . For multiple classification, we use macro average of the auPRC and auROC  
565 to evaluate the classification performance, which compute the metric independently for each  
566 class and then take the average hence treating all classes equally. For regression design, we  
567 used two metrics for model evaluation, which are cell-type-wise Pearson correlation coefficient  
568 and prediction squared error. Prediction square error (PSR) is calculated as  $PSR = 1 -$   
569  $\sum_k \sum_i (y_{ik} - \hat{y}_{ik})^2 / (y_{ik} - \bar{y}_{*k})^2$ , where  $\bar{y}_{*k} = \sum_l y_{lk} / L$  denotes the mean of the true level of  
570 the response in the cell type k.

571 To compare the performance of our method with other baseline methods, we conducted  
572 hypothesis testing on the metrics based on cell types. Since the metrics on a given cell type  
573 across different methods are paired data and the statistical distribution is unknown, we  
574 employed both Binomial and Wilcoxon tests, with the alternative hypothesis being that  
575 EpiGePT outperforms the other methods. If we reject the null hypothesis, it provides  
576 compelling evidence to support the claim that EpiGePT performs better than the other methods.

577 To evaluate the computational efficiency, we recorded the running time of a single epoch of  
578 EpiGePT and baseline methods (Supplementary Text S3). Compared to traditional CNN models  
579 such as DeepCAGE<sup>17</sup> and ChromDragoNN<sup>16</sup>, as well as larger sequence models like Enformer,  
580 EpiGePT demonstrates a balance between high computational efficiency and performance.

### 581 **Model fine-tuning**

582 For the fine-tuning process, we kept the parameters of the pre-trained model fixed without  
583 making any updates. For the specific fine-tuning task of chromatin interaction prediction based

584 on HiChIP data, the multi-task module was replaced with a two-layer MLP network, containing  
585 256 hidden nodes for each layer. During the training process, only the weights in the MLP  
586 network were updated. Notably, when utilizing HiChIP data at a resolution of 5k, both the  
587 enhancer and promoter anchors spanned 5kbp. Then we input a region extending 128kbp from  
588 the center of the anchor of the neighboring gene into the EpiGePT. Consequently, a 968-  
589 dimensional feature vector for each genomic bin was derived from the output of the last  
590 transformer encoder layer. These feature vectors from all bins within the two anchors were  
591 concatenated, resulting in a high-dimensional vector of size 76,472.

## 592 **Baseline methods**

593 Four baselines were introduced for epigenetic signals prediction. BIRD<sup>15</sup> is a multiple linear  
594 regression model that only takes gene expression data as input and makes predictions on a fixed  
595 locus. ChromDragoNN<sup>16</sup> is a deep neural network that takes gene expression of 1630 TFs and  
596 DNA sequence as input. Specifically, ChromDragoNN<sup>16</sup> uses a ResNet<sup>52</sup> to extract sequence  
597 features and use linear transformation to combine the TF gene expression feature and sequence  
598 feature to make the final prediction. DeepCAGE<sup>17</sup> Integrating regulatory DNA sequence is a  
599 deep densely connected convolutional network for predicting chromatin accessibility. The  
600 dense-connected neural network architecture used by DeepCAGE<sup>17</sup> may struggle to capture the  
601 complex interactions between genomic regions. Enformer<sup>11</sup> is a deep neural network that  
602 integrates convolutional neural network and transformer, and only takes DNA sequence as input.  
603 Enformer takes DNA sequence of length 196kbp as input to predict 5,313 genomic tracks of  
604 human and 1,643 tracks of mouse genome simultaneously. However, one of the limitations of  
605 Enformer is that it can only model and predict cell types in the training data and cannot be

606 applied to new cell types. In order to ensure the fairness of the benchmark experiment, we  
607 retrained the Enformer model with the same input and output data as EpiGePT when reproduce  
608 the Enformer model (Text S4).

609 Two baseline methods were introduced for predicting HiChIP interaction. DeepTACT<sup>39</sup> is a  
610 deep learning method for predicting 3D chromatin contacts using both DNA sequence and  
611 chromatin accessibility. We adopted the structure of DeepTACT<sup>39</sup> and kept the anchor length at  
612 5k. The input to the model consists of two anchor sequences represented as one-hot matrices  
613 and the two openness scores of the two anchors on the corresponding cell type extracted from  
614 OpenAnnotate<sup>53</sup>. Regarding the Kmer features<sup>40</sup>, K is chosen as 5 to extract sequence features.  
615 For each anchor, a vector of dimension  $4^5 = 1024$  was obtained. Further training was  
616 performed using an MLP with a hidden layer dimension of 256.

## 617 **Enhancer, Silencer and HiChIP loop prioritization**

618 We collected cis-regulatory elements-gene pairs in K562 cells from other studies and public  
619 database to demonstrate the interpretability of self-attention mechanisms in the EpiGePT.  
620 Enhancers and silencers are typical *cis*-regulatory elements known play important roles in  
621 transcriptional control during normal development and disease. For enhancers, we downloaded  
622 enhancer-gene pairs from two studies: Gasperini et al.<sup>23</sup> and Fulco et al.<sup>24</sup>, both of which were  
623 tested using a CRISPRi<sup>22</sup> assay perturbation. Two datasets contain 664 and 5,091 enhancer-  
624 promoter interactions or element-TSS interactions. For silencers, we obtained and random  
625 sampled 831 validated silencers-gene pairs with distance within 64kbp in K562 cells curated  
626 from high-throughput experiments from SilencerDB. As there are no experimentally validated

627 interaction relationships between these silencers and genes, we generated silencer-gene pairs  
628 by associating the nearest neighbor genes for classification purposes. Similarly, negative  
629 samples were generated by constructing DNase-seq, ATAC-seq and nearest genes using the  
630 same approach. Ultimately, we obtained a dataset comprising 1,662 silencer-gene pairs,  
631 encompassing both positive and negative instances.

632 To obtain scores for regulatory element-gene pairs, we first used the region extending 128kbp  
633 from the center of the enhancer as input and extracted the token where the interacting genes  
634 reside, so that we could filter out regulatory element-gene pairs that were located further than  
635 64kbp apart. Subsequently, we stratified the remaining pairs based on their distance. Since the  
636 positive and negative sample ratios varied across datasets, we adopted different stratification  
637 strategies for different distance ranges (**Fig. 3**). Next, we averaged the attention matrices of the  
638 Transformer encoder across all layers and heads. The summed attention scores from other  
639 tokens to the key token containing the gene TSS were used as the attention score of this element-  
640 gene pair. This score represents the attention value that the enhancer-centered region receives  
641 for the transcription start site (TSS) of the gene. We also calculated the attention score from the  
642 bin containing the center of the regulatory element to the bin containing the TSS, which only  
643 slightly affects the experimental results of regulatory element prioritization.

644 We collected 5k resolution data from the HiChIPdb (<http://health.tsinghua.edu.cn/hichipdb/>)  
645 database, specifically from K562 and GM12878 cell lines. We filtered the data to include only  
646 loops where at least one anchor falls within a gene region. We stratified the loops based on  
647 distance into three categories: 0-20kbp, 20-40kbp, and 40-64kbp. For each distance category,  
648 we selected 2000 positive pairs with most significant q-value. To ensure consistency in the

649 distance distribution, we selected negative pairs by fixing a gene and choosing anchors at  
650 equidistant locations in the opposite direction.

## 651 **Gradient importance scores**

652 EpiGePT possesses the capability to assign priority rankings to transcription factors by utilizing  
653 gradient importance scores (GIS), taking into account specific cell types and chromatin regions.  
654 The GIS were employed to identify potential functional relationships between specific  
655 transcription factors (TFs) and target genes. Specifically, for a given TF-target gene pair, the  
656 transcription start sites (TSS) of genes were used as central loci, and the regions spanning 128  
657 kbp upstream and downstream of the TSS were selected as input. Next, we filtered out bins  
658 with motif binding scores indicating potential binding for the given TF. For these selected bins,  
659 we calculated the GIS for the predictions of eight epigenomic signals across the 711 core TFs.

$$660 \quad GIS_{ijk} = \frac{1}{|\zeta|} \sum_{l \in \zeta} \left| \frac{\partial \hat{y}_{ljk}}{\partial t_{f_{ij}}} \right|$$

661 Where,  $i$  denotes the  $i$ th TF in the set of core TFs,  $j$  denotes the  $j$ th cell type,  $k$  denotes the  $k$ th  
662 predicted epigenomic signal, and  $\zeta$  denotes the set of genomic bins that have binding for the  
663 given TF. In the calculation of the gradient,  $\hat{y}_{ljk}$  denotes the predicted value of the  $k$ th  
664 epigenomic signal by the model using the expression in the  $j$ th cell type at the  $l$ th bin. On the  
665 other hand,  $t_{f_{ij}}$  denotes the product of the expression of  $i$ th TF in the  $j$ th cell type and the  
666 corresponding TF binding score.

667 If we consider the GIS for the prediction of all 8 epigenomic signals simultaneously, we can  
668 prioritize the TFs by calculating their ranks based on each signal separately. Then, we can



669 calculate an integrated gradient importance score (IGIS) for each TF by aggregating the ranks  
670 from all 8 signals.

$$671 \quad IGIS_{ij} = \frac{1}{8} \sum_k rank(GIS_{ijk})$$

672 Both the GIS and the IGIS are capable of capturing the significance of a transcription factor  
673 (TF) in regulating a specific gene within the context of a specific cell type. Consequently, these  
674 scores hold potential value in the discovery of TFs that play crucial roles in the regulation of  
675 specific genes, thereby contributing to our understanding of essential regulatory mechanisms.

676 In the context of validating TF-TG pairs in the GRNdb and TRRUST databases, we opted to  
677 utilize liver expression data as a representative example due to the unavailability of cell type  
678 information for TRRUST. Furthermore, in this experimental setup, the  $tf_{ij}$  denotes the  
679 expression of  $i$ th TF in the  $j$ th cell type and  $\zeta$  denotes the set of genomic bins that have binding  
680 for the TF of the given TF-target gene pair.

### 681 **Potential TF-target gene pairs from ChIP-seq data**

682 In this study, we utilized three distinct cell types to conduct a comprehensive screening of TF-  
683 target gene pairs and non-target gene pairs across the human genome. Initially, we obtained the  
684 narrow peak files (ENCFF388AJH, ENCFF717IXP, and ENCFF885KLR) from ChIP-seq  
685 experiments across three cell types from the ENCODE project. Subsequently, we meticulously  
686 examined the number of peaks within a 128kbp region both upstream and downstream of the  
687 transcription start site (TSS) for each gene. Different thresholds were applied to the ChIP-seq  
688 data of various TFs. Genes lacking any peaks within the defined region were classified as non-

689 target genes, while genes surpassing the threshold in terms of peak counts were designated as  
690 target genes. Specifically, for the aforementioned three cell types, threshold values of 10, 15,  
691 and 6 were respectively employed. Finally, the IGIS approach was employed to determine the  
692 corresponding ranks of TFs in the TF-target gene pairs.

### 693 **Pathogenic SNPs prioritization**

694 We collected single nucleotide polymorphisms (SNPs) data from the ClinVar and ExAC  
695 databases, which include both potentially pathogenic and benign SNPs. To evaluate the ability  
696 of EpiGePT to predict variant effects, we computed the log-odds scores (LOS) for multiple  
697 chromatin signals using EpiGePT on these SNPs. Subsequently, we utilized these scores to  
698 distinguish between pathogenic and benign SNPs. The LOS score for each chromatin signal  
699 was defined by computing a forward pass through the model using the reference and alternative  
700 alleles.

$$701 \quad \Delta O_{signal} = \log \left( \frac{output(I_{alt})}{output(I_{ref})} \right)$$

702 Each chromatin epigenomic profile in each cell line or tissue predicted by EpiGePT can be used  
703 to compute a specific variant score. We did not take the absolute value in this calculation, so  
704 the resulting LOS score indicates the direction of change in the model output after the  
705 appearance of the variant. In addition to the predicted chromatin signals output by the eight  
706 models, attention score changes based on self-attention are also noteworthy. We computed the  
707 log-odds scores for attention by summing the attention scores of the 10 bins upstream and  
708 downstream of the locus of the SNP, to evaluate the effect of the variant.

$$\Delta O_{attention} = \sum_{i=-5}^5 \left| \log \left( \frac{attn(bin_i)_{I(alt)}}{attn(bin_i)_{I(ref)}} \right) \right|$$

709  
710 Where  $i$  represents the index of the neighboring bins relative to the locus of the SNP. To avoid  
711 the variant effects of different bins from cancelling each other out during the summation process,  
712 we computed the absolute value of the change in attention scores for each bin and then summed  
713 the scores of the 10 adjacent bins centered at the SNP position. For the classification of  
714 pathogenic SNPs, we calculated these nine LOS for attention separately for each of the 28  
715 tissues or cell lines in training data. As a result, we obtained a feature vector of 252 dimensions  
716 for each SNP. Then a classifier with 252 features computed by EpiGePT and 52 annotations  
717 from CADD score as inputs are used to predict pathogenic SNPs against benign or likely benign  
718 SNPs. Here, we employed MLP as classifier to validate the effectiveness of the features we  
719 obtained. A five-fold cross-validation experiment is employed for validation, and we utilize two  
720 different positive-to-negative sample ratios, namely 1:1 and 1:2. For each sample ratio, we  
721 randomly sample 32,000 positive samples. The effectiveness of the variant score in identifying  
722 pathogenic SNPs is evaluated using the area under the auROC and the auPRC. Additionally,  
723 we also utilized the logistic regression (LR) as the classifier, consistent with the LR classifier  
724 used in CADD, and found a similar improvement when predicting pathogenic SNPs.

725 We applied the same method to calculate the LOS scores of the 8 predicted chromatin signals  
726 for the COVID-19 GWAS data. The absolute values of the scores were summed as the overall  
727 score for each SNP. For each significant SNP associated with COVID-19 severity obtained  
728 from the GWAS data, we selected normal SNPs within a 64kb region around the SNP as  
729 background to calculate the rank of the LOS score for the COVID-19 associated SNP in this

730 region. Furthermore, we calculated the LOS scores for all 9, 484 COVID-19 associated SNPs  
731 and ranked them accordingly. The top 10 SNPs with the highest LOS scores were selected,  
732 which are considered to have potential genetic associations with COVID-19 severity and  
733 complications.

### 734 **GTEx classification**

735 We collected eQTL data from the supplementary materials of Wang et al<sup>28</sup>. In their study, the  
736 authors identified causal eQTLs through statistical fine-mapping, using a posterior inclusion  
737 probability (PIP) threshold of >0.9 for putative causal variants based on expression modifier  
738 score (EMS), and a PIP threshold of <0.9 for putative non-causal variants. To validate the ability  
739 of EpiGePT to distinguish potential causal variants, we perform a classification task on these  
740 variants. For each variation, 128kbp sequence regions near it were selected as the input of the  
741 model, and a score of variation was given by EpiGePT model. For each variant under each  
742 tissue, we can obtain an 8-dimensional vector of genomic features including DNase, CTCF and  
743 other ChIP-seq signals. Based on the LOS score, separate random forest classifiers consisting  
744 of 10 decision trees are trained for each tissue in order to distinguish between causal and non-  
745 causal variants. The models are evaluated using 5-fold validation on each tissue, with area under  
746 the auPRC and auROC as metrics for assessing their ability to distinguish between causal and  
747 non-causal variants.

### 748 **Code availability**

749 All components of EpiGePT are freely available at <https://github.com/ZjGaothu/EpiGePT>.

750 Here, users can access the code for reproducing EpiGePT, as well as the data collection and  
751 preprocessing pipelines used for model training in benchmark experiments.

## 752 **Data availability**

753 Information and processed data of multiple chromatin signals of whole genome, motif binding  
754 status and expression data of TFs in the corresponding cell lines/tissues, which are used in  
755 EpiGePT are available at Supplementary Tables. The information about the cell lines/tissues  
756 used and the 711 filtered transcription factors is available in the supplementary table. The High  
757 throughput validated silencers of K562 cell line are download from SilencerDB  
758 (<http://health.tsinghua.edu.cn/silencerdb>) database. The HiChIP data of K562 cell line and  
759 GM12878 cell line are downloaded from HiChIPdb (<http://health.tsinghua.edu.cn/hichipdb/>)  
760 database. The DNase-seq peak and ATAC-seq peak data are obtained from the ENCODE  
761 project. Enhancer-gene pairs of CRISPRi<sup>24</sup> experiments are obtained from the supplementary  
762 information of Gasperini et al. and Fulco et al. The regulatory network data for transcription  
763 factors and target genes were obtained from the TRRUST<sup>47</sup> database  
764 (<https://www.grnpedia.org/trrust/>) and the GRNdb<sup>46</sup> database (<http://www.grndb.com>). The  
765 annotated chromatin states for whole genome are downloaded from the ROADMAP  
766 epigenomics project ([https://egg2.wustl.edu/roadmap/web\\_portal/chr\\_state\\_learning.html](https://egg2.wustl.edu/roadmap/web_portal/chr_state_learning.html)).  
767 The RNA-seq read counts matrix for protein coding genes used for the prediction of the  
768 chromatin 15-states annotated by ChromHMM are downloaded from the ROADMAP project  
769 (<https://egg2.wustl.edu/roadmap/data/byDataType/rna/expression/57epigenomes.N.pc.gz>).  
770 The GWAS data of COVID-19 are download from the COVID-19 Host Genetics Initiative  
771 (<https://www.covid19hg.org/>).

772 **Competing interests**

773 The authors have declared no competing interests.

774 **Acknowledgments**

775 Z.G and R.J. was supported by the National Key Research and Development Program of China

776 [2021YFF1200902] and the National Natural Science Foundation of China [62203236 and

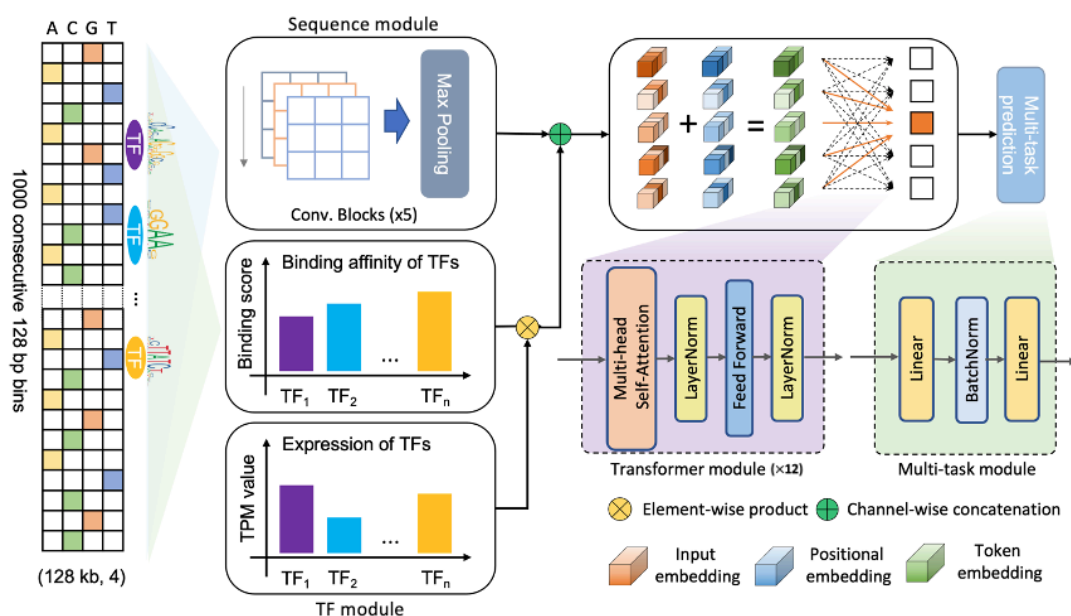
777 62273194]. Q.L., W.Z and W.H.W were supported by NIH grants R01 HG010359, P50

778 HG007735 and NSF DMS 1952386.

779

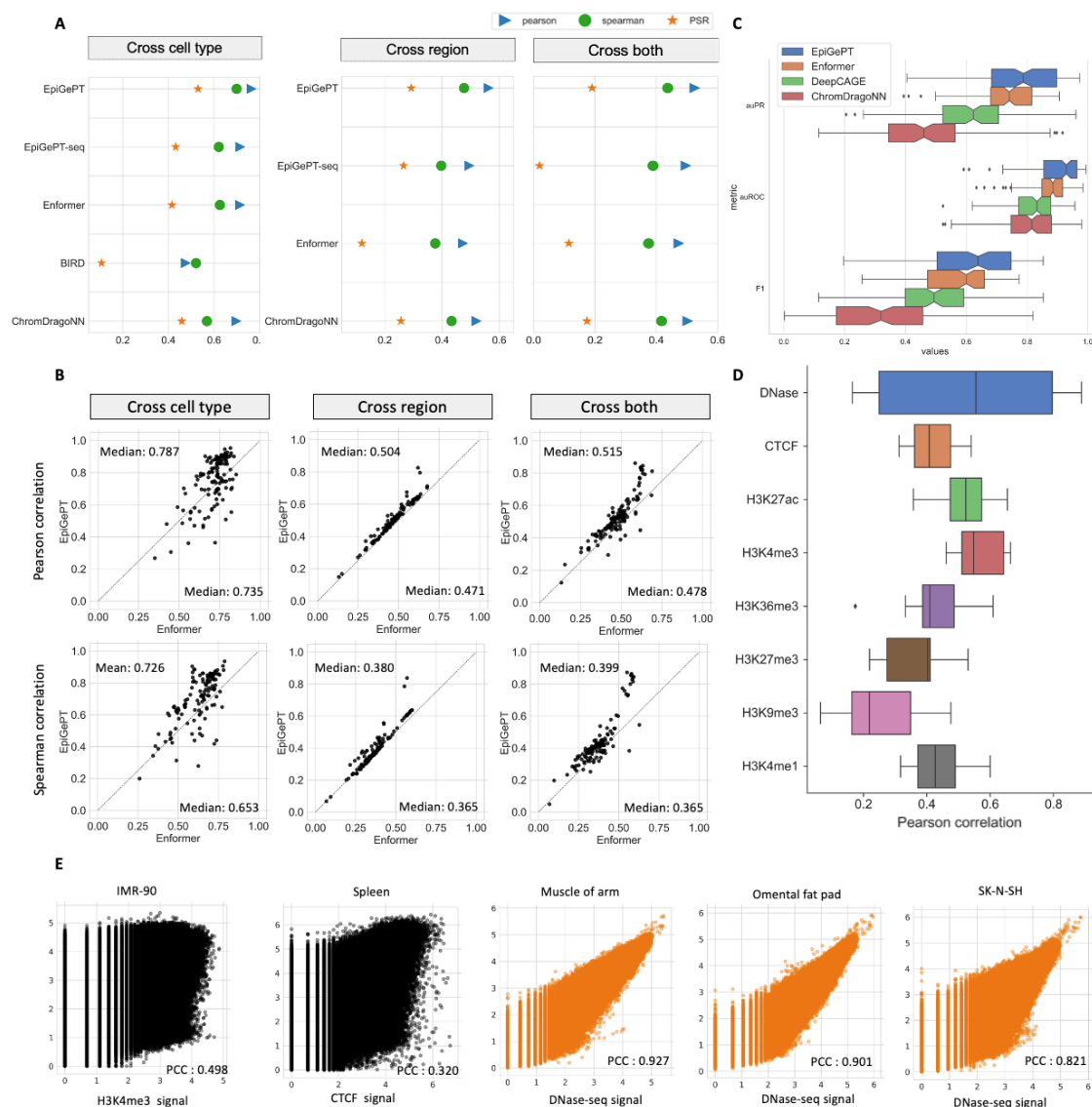
780 **Figures**

781 **Figure 1**



782 **Fig. 1 Overview of the EpiGePT model for multiple epigenomic signals prediction.** The  
 783 model consists of four modules, namely the Sequence module, the TF module, the Transformer  
 784 module, and the Multi-task module. The sequence module comprises multiple layers of  
 785 convolution applied to the one-hot encoded DNA sequence input. The input sequence length  
 786 consists of 1000 genomic bins of 128bp for the prediction of multiple signals and 50 bins of  
 787 200bp for the prediction of DNase signal alone. The TF module encompasses the binding status  
 788 and expression of 711 transcription factors. The Transformer module consists of a series of  
 789 consecutive transformer encoders, while the multi-task module is composed of a fully  
 790 connected layer.

791 **Figure 2**



792 **Fig. 2 Performance of EpiGePT and baseline methods on the benchmark experiment. (A)**

793 EpiGePT and baseline methods were compared in terms of their regression performance for

794 DNase signal regression across cell types, genomic regions, and combined cell type and

795 genomic regions. (B) Comparison of EpiGePT and Enformer performance. Each point in the

796 scatter plot represents the performance of Enformer on the data of a specific cell type (x-axis)

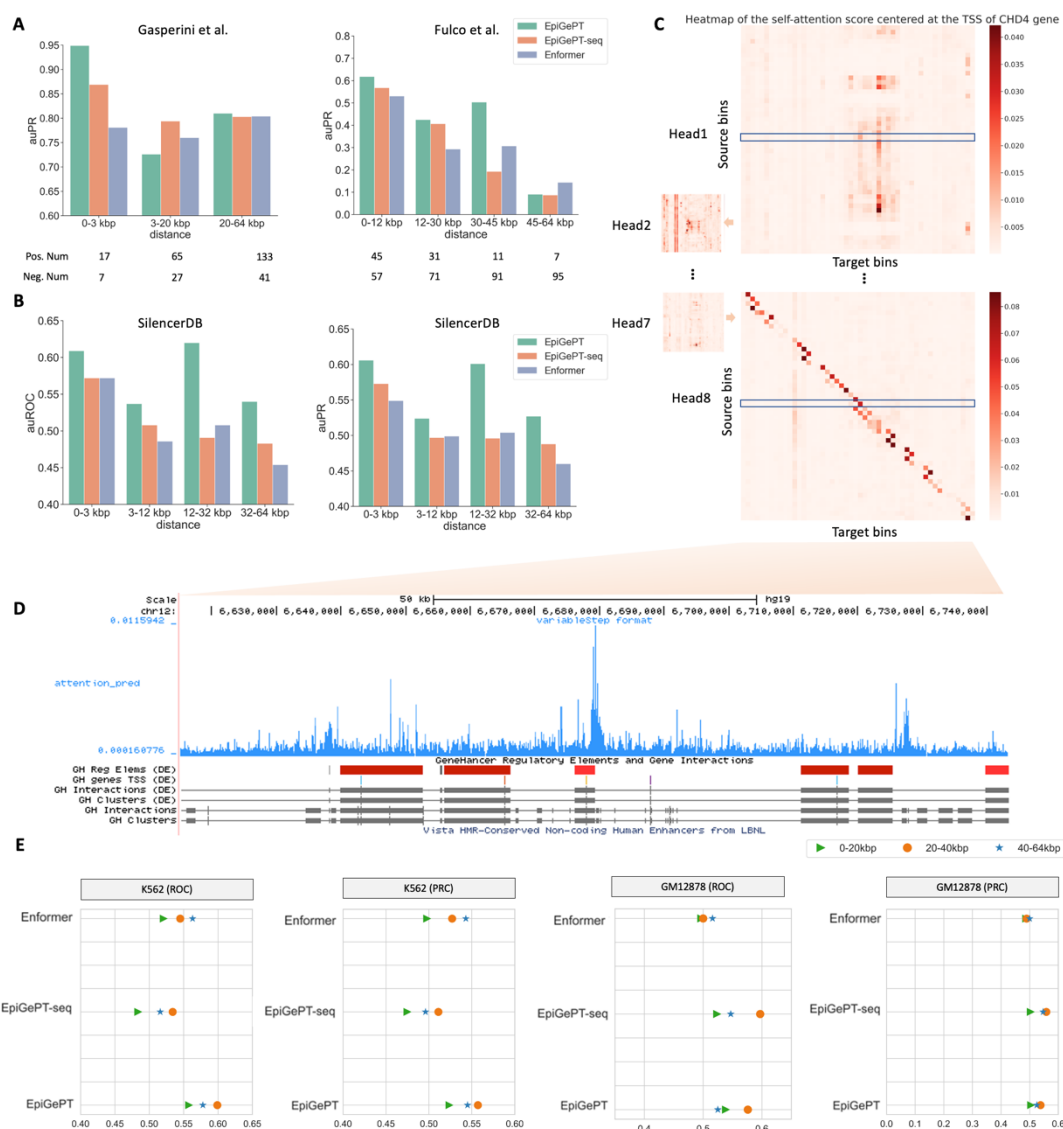
797 compared to the performance of EpiGePT (y-axis). (C) EpiGePT and baseline methods'

798 performance on binary prediction of DNase-seq signals. (D) EpiGePT demonstrates excellent



799 performance in predicting diverse epigenetic signals across various cell types, including  
800 DNase-seq, CTCF, and histone modifications. (E) EpiGePT predictions compared to  
801 experimental signals visualized for a representative example. Genome-wide multi-signal  
802 predictions (black) and DNase-specific predictions (orange).

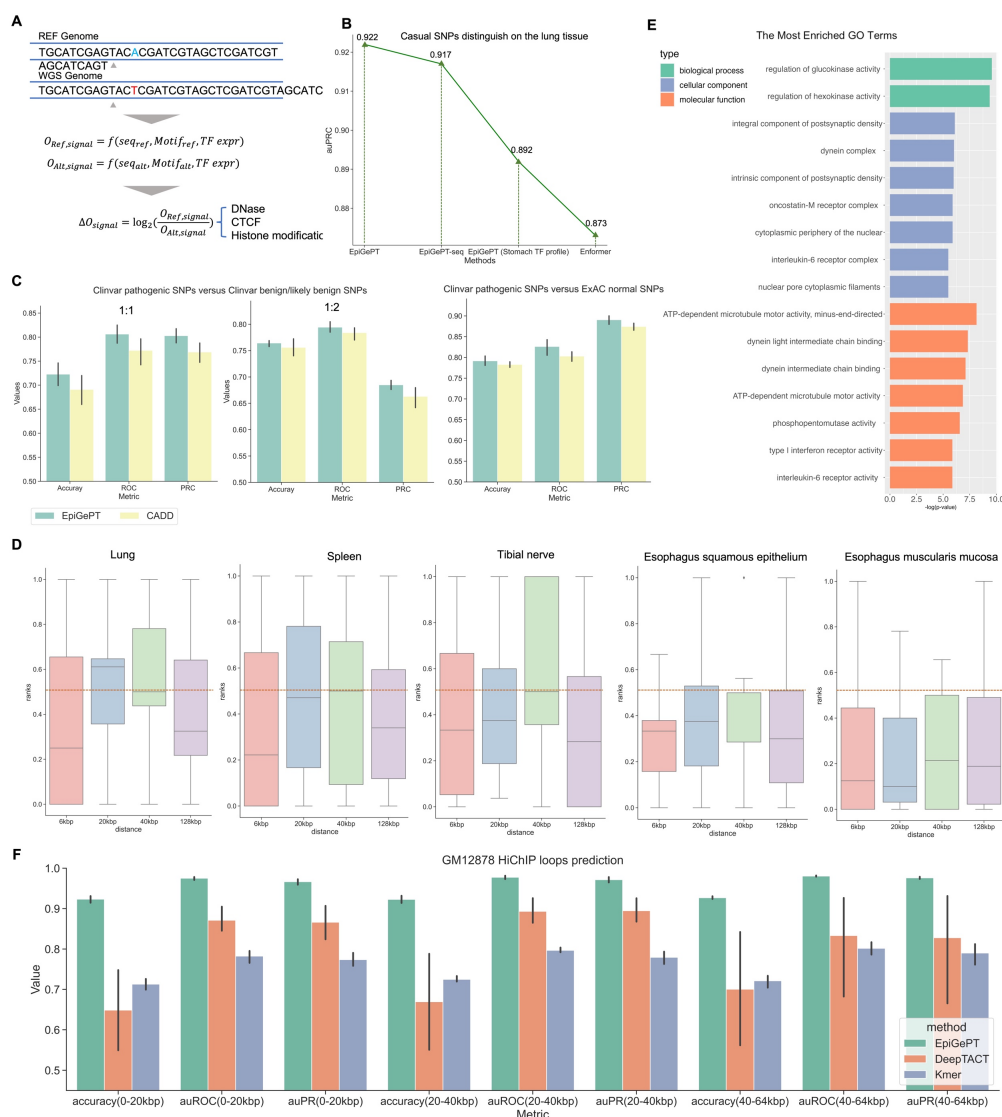
**Figure 3**



803 **Fig. 3 Application of self-attention mechanism in EpiGePT for long-range chromatin**  
 804 **interaction identification.** (A) The performance (auPRC) of attention score of EpiGePT in  
 805 distinguishing enhancer-gene pairs at different distance ranges on two different datasets. (B)  
 806 The performance (auROC and auPRC) of attention score of EpiGePT in distinguishing silencer-  
 807 gene pairs at different distance ranges based on the data from SilencerDB<sup>25</sup>. (C) Heatmap of  
 808 the self-attention matrix of each attention head centered at the TSS of the CHD4 gene, the  $(i, j)$   
 809 element in the matrix denotes the average attention score between the  $i$ th genomic bin and the

810  $j$ th genomic bin across all layers. (D) Attention scores centered at the TSS of the CHD4 gene,  
811 and putative enhancer regions in its vicinity. (E) The performance (auROC and auPRC) of  
812 attention score of EpiGePT in distinguishing HiChIP loops of H3K27ac at different distance  
813 ranges on K562 cell line and GM12878 cell line.

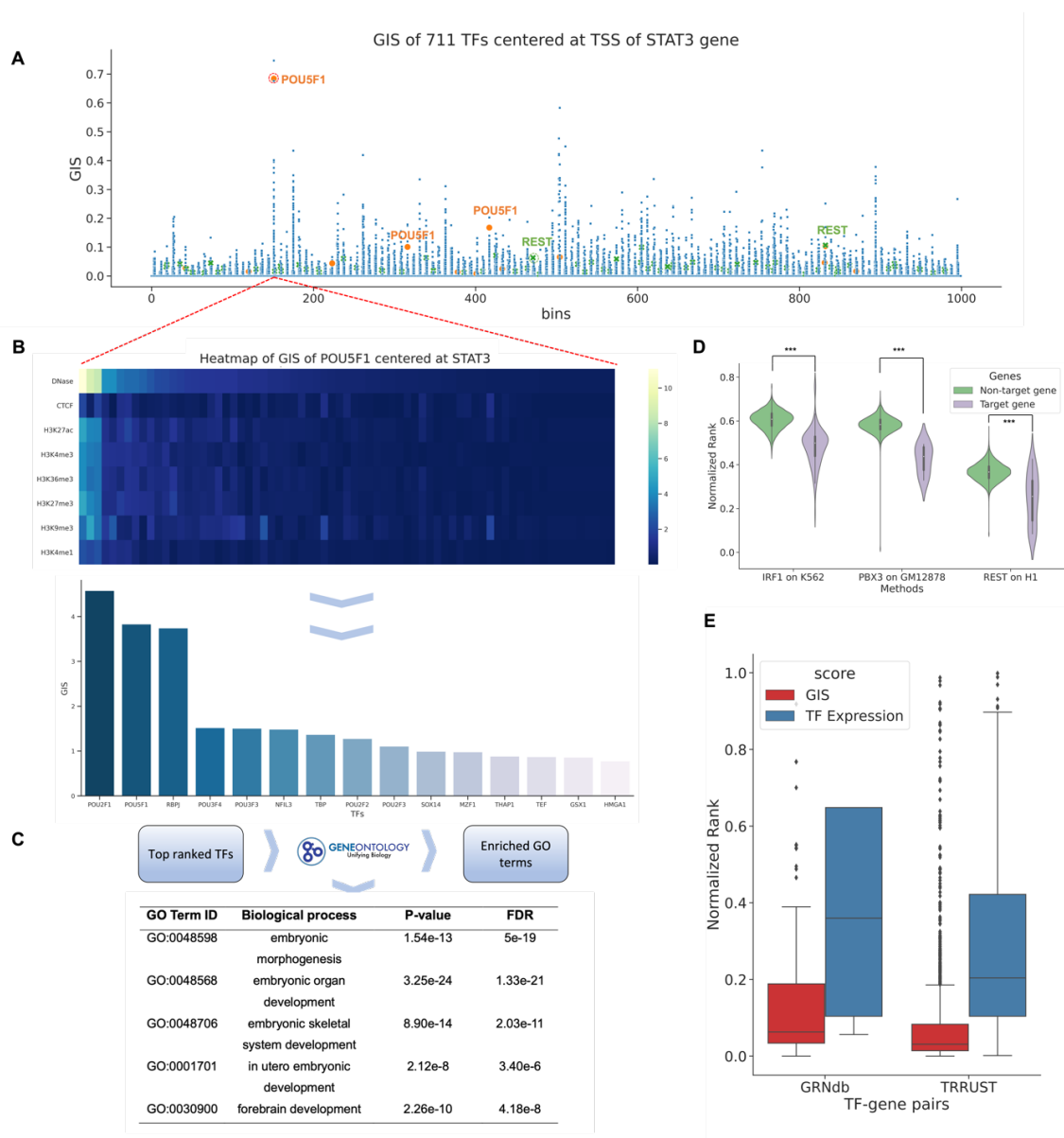
814 **Figure 4**



815 **Fig. 4 Variant effect prediction of EpiGePT.** (A) The LOS score for each epigenomic signal  
 816 is calculated by the log change fold of the predicted epigenomic signal for reference genome  
 817 and WGS genome. (B) The performance of EpiGePT and Enformer in discriminating causal  
 818 SNPs on the Lung tissue. (C) The three subplots from left to right respectively depict the  
 819 classification results for disease-related SNPs and benign SNPs down-sampled sourced from  
 820 the ClinVar database, with balanced positive and negative samples (1:1 and 1:2 ratio), as well

821 as normal SNPs sourced from the ExAC database with a MLP classifier. (D) The ranked  
822 position of COVID-19 related GWAS data among surrounding benign SNPs based on their  
823 LOS scores, as determined using different tissue or cell-type expression data. The results were  
824 stratified based on the distance range of the risk region. The resulting mean and median ranks  
825 were both below 0.5. (E) Enrichment result (Biological process, Cellular component and  
826 Molecular function) of the nearest genes of the COVID-19 associated SNPs with the max LOS  
827 scores. (F) The performance (auROC and auPRC) of the fine-tuned EpiGePT model and  
828 baseline methods (DeepTACT and Kmer) in distinguishing enhancer-gene pairs at various  
829 distance ranges (0-20 kbp, 20-40 kbp and 40-64 kbp) on K562 cell line.

830 **Figure 5**



831 **Fig. 5 Gradient importance scores (GIS) uncover regulatory transcription factors. (A)**

832 Genomic regions around TSS of the STAT3 gene and expression data on ESC were fed into

833 EpiGePT. The scatter plot represents the GIS scores of core TFs on each genomic bin. Each dot

834 represents the GIS score of a core TF on a specific genomic bin. In specific bins, key TFs in

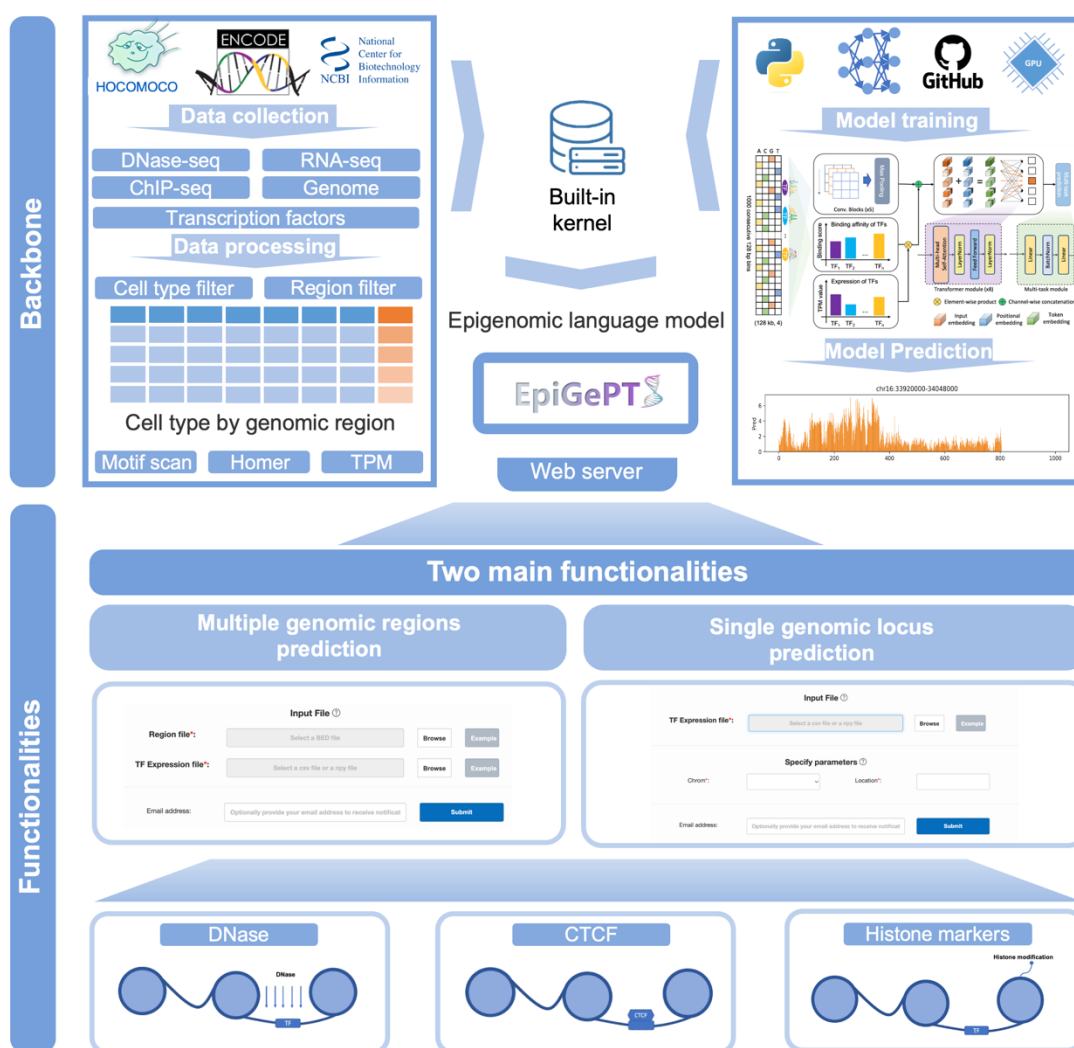
835 ESC, such as NR5A2 and POU1F5 highlighted in the figure, exhibit high ranks in the GIS

836 scores. (B) Heatmap of GIS for 10% important TFs surrounding STAT3 gene, specifically

837 focusing on bins with POU1F5 ranked 3rd. Each row represents a predicted epigenomic signal,

838 and the TFs are sorted based on their GIS on DNase signals. Bar plot of the top 15 TFs with the  
839 highest GIS scores. (C) Based on the top 10% ranked TFs mentioned above, gene ontology  
840 enrichment analysis revealed significant enrichment in biological processes related to  
841 embryonic development and cellular differentiation. (D) Based on TF ChIP-seq data, all 23,635  
842 human genes were classified into target genes and non-target genes. The results revealed that  
843 TFs exhibited significantly higher ranks on potential target genes compared to non-target genes.  
844 (E) The distribution of the rank of TFs in the GIS and expression value among the 2,705 TF-  
845 gene pairs from the TRRUST database and 1,066 TF-gene pairs derived from genotype-tissue  
846 expression (GTEx) data of the liver sourced from the GRNdb database. The analysis reveals  
847 that the median rank of TFs from the TRRUST database is significantly lower than 0.06 (one-  
848 side  $p$ -value  $< 3.12 \text{ e-}18$ ) and the median rank of TFs obtained from the GRNdb database is  
849 significantly lower than 0.5 (one-side  $p$ -value  $< 2.50 \text{ e-}140$ ).

850 **Figure 6**



851 **Fig. 6 Overview of the online prediction web server of EpiGePT.** We collected eight types  
 852 of epigenetic genome modification signals and corresponding expression data of transcription  
 853 factors in different cell types or tissues from the ENCODE project. Based on these data, we  
 854 trained the EpiGePT model and deployed it as a built-in kernel on an Apache server. Users  
 855 without much coding experience can also access the web server in two ways to obtain the eight  
 856 types of epigenetic genome modification signals for specified cell types and genomic regions  
 857 without programming or installation.

858



## 859 Reference

- 860 1. Brown, T. et al. Language models are few-shot learners. *Advances in neural information*  
861 *processing systems* **33**, 1877-1901 (2020).
- 862 2. Ramesh, A. et al. in International Conference on Machine Learning 8821-8831 (PMLR, 2021).
- 863 3. Alexander, R.P., Fang, G., Rozowsky, J., Snyder, M. & Gerstein, M.B. Annotating non-coding  
864 regions of the genome. *Nature Reviews Genetics* **11**, 559-571 (2010).
- 865 4. O'Malley, R.C. et al. Cistrome and episcistrome features shape the regulatory DNA landscape.  
866 *Cell* **165**, 1280-1292 (2016).
- 867 5. Yenduri, G. et al. Generative Pre-trained Transformer: A Comprehensive Review on Enabling  
868 Technologies, Potential Applications, Emerging Challenges, and Future Directions. *arXiv*  
869 *preprint arXiv:2305.10435* (2023).
- 870 6. Liu, Q., Xia, F., Yin, Q. & Jiang, R. Chromatin accessibility prediction via a hybrid deep  
871 convolutional neural network. *Bioinformatics* **34**, 732-738 (2018).
- 872 7. Min, X., Zeng, W., Chen, N., Chen, T. & Jiang, R. Chromatin accessibility prediction via  
873 convolutional long short-term memory networks with k-mer embedding. *Bioinformatics* **33**,  
874 i92-i101 (2017).
- 875 8. Yin, Q., Wu, M., Liu, Q., Lv, H. & Jiang, R. DeepHistone: a deep learning approach to  
876 predicting histone modifications. *BMC genomics* **20**, 11-23 (2019).
- 877 9. Liu, Q., Lv, H. & Jiang, R. hicGAN infers super resolution Hi-C data with generative adversarial  
878 networks. *Bioinformatics* **35**, i99-i107 (2019).
- 879 10. Zeng, W., Wu, M. & Jiang, R. Prediction of enhancer-promoter interactions via natural language  
880 processing. *BMC Genomics* **19**, 84 (2018).
- 881 11. Avsec, Ž. et al. Effective gene expression prediction from sequence by integrating long-range  
882 interactions. *Nature methods* **18**, 1196-1203 (2021).
- 883 12. Consortium, E.P. An integrated encyclopedia of DNA elements in the human genome. *Nature*  
884 **489**, 57 (2012).
- 885 13. Vaswani, A. et al. in Advances in neural information processing systems 5998-6008 (2017).
- 886 14. Song, L. & Crawford, G.E. DNase-seq: a high-resolution technique for mapping active gene  
887 regulatory elements across the genome from mammalian cells. *Cold Spring Harbor Protocols*

- 888           **2010**, pdb. prot5384 (2010).
- 889   15.   Zhou, W. et al. Genome-wide prediction of DNase I hypersensitivity using gene expression.  
890       *Nature communications* **8**, 1-17 (2017).
- 891   16.   Nair, S., Kim, D.S., Perricone, J. & Kundaje, A. Integrating regulatory DNA sequence and gene  
892       expression to predict genome-wide chromatin accessibility across cellular contexts.  
893       *Bioinformatics* **35**, i108-i116 (2019).
- 894   17.   Liu, Q., Hua, K., Zhang, X., Wong, W.H. & Jiang, R. DeepCAGE: incorporating transcription  
895       factors in genome-wide prediction of chromatin accessibility. *Genomics, Proteomics &*  
896       *Bioinformatics* **20**, 496-507 (2022).
- 897   18.   Holwerda, S.J.B. & de Laat, W. CTCF: the protein, the binding partners, the binding sites and  
898       their chromatin loops. *Philosophical Transactions of the Royal Society B: Biological Sciences*  
899       **368**, 20120369 (2013).
- 900   19.   Bannister, A.J. & Kouzarides, T. Regulation of chromatin by histone modifications. *Cell*  
901       *research* **21**, 381-395 (2011).
- 902   20.   Karolchik, D. et al. The UCSC genome browser database. *Nucleic acids research* **31**, 51-54  
903       (2003).
- 904   21.   Ernst, J. & Kellis, M. Chromatin-state discovery and genome annotation with ChromHMM.  
905       *Nature protocols* **12**, 2478-2492 (2017).
- 906   22.   Larson, M.H. et al. CRISPR interference (CRISPRi) for sequence-specific control of gene  
907       expression. *Nature protocols* **8**, 2180-2196 (2013).
- 908   23.   Gasperini, M. et al. A genome-wide framework for mapping gene regulation via cellular genetic  
909       screens. *Cell* **176**, 377-390. e319 (2019).
- 910   24.   Fulco, C.P. et al. Activity-by-contact model of enhancer–promoter regulation from thousands  
911       of CRISPR perturbations. *Nature genetics* **51**, 1664-1669 (2019).
- 912   25.   Zeng, W. et al. SilencerDB: a comprehensive database of silencers. *Nucleic acids research* **49**,  
913       D221-D228 (2021).
- 914   26.   Mumbach, M.R. et al. HiChIP: efficient and sensitive analysis of protein-directed genome  
915       architecture. *Nature methods* **13**, 919-922 (2016).
- 916   27.   Zeng, W., Liu, Q., Yin, Q., Jiang, R. & Wong, W.H. HiChIPdb: a comprehensive database of  
917       HiChIP regulatory interactions. *Nucleic Acids Research* **51**, D159-D166 (2023).

- 918 28. Wang, Q.S. et al. Leveraging supervised learning for functionally informed fine-mapping of cis-  
919 eQTLs identifies an additional 20,913 putative causal eQTLs. *Nature Communications* **12**, 3394  
920 (2021).
- 921 29. Landrum, M.J. et al. ClinVar: public archive of interpretations of clinically relevant variants.  
922 *Nucleic acids research* **44**, D862-D868 (2016).
- 923 30. Karczewski, K.J. et al. The ExAC browser: displaying reference data information from over 60  
924 000 exomes. *Nucleic acids research* **45**, D840-D845 (2017).
- 925 31. Rentzsch, P., Witten, D., Cooper, G.M., Shendure, J. & Kircher, M. CADD: predicting the  
926 deleteriousness of variants throughout the human genome. *Nucleic acids research* **47**, D886-  
927 D894 (2019).
- 928 32. Li, J., Lai, S., Gao, G.F. & Shi, W. The emergence, genomic diversity and global spread of  
929 SARS-CoV-2. *Nature* **600**, 408-418 (2021).
- 930 33. org, C.-H.G.I.a.b. The COVID-19 host genetics initiative, a global initiative to elucidate the role  
931 of host genetic factors in susceptibility and severity of the SARS-CoV-2 virus pandemic.  
932 *European Journal of Human Genetics* **28**, 715-718 (2020).
- 933 34. Agius, L. Targeting hepatic glucokinase in type 2 diabetes: weighing the benefits and risks.  
934 *Diabetes* **58**, 18-20 (2009).
- 935 35. Singh, A.K., Gupta, R., Ghosh, A. & Misra, A. Diabetes in COVID-19: Prevalence,  
936 pathophysiology, prognosis and practical considerations. *Diabetes & Metabolic Syndrome:  
937 Clinical Research & Reviews* **14**, 303-310 (2020).
- 938 36. Pellegrina, D., Bahcheli, A.T., Krassowski, M. & Reimand, J. Human phospho-signaling  
939 networks of SARS-CoV-2 infection are rewired by population genetic variants. *Molecular  
940 Systems Biology* **18**, e10823 (2022).
- 941 37. Radford, A., Narasimhan, K., Salimans, T. & Sutskever, I. Improving language understanding  
942 by generative pre-training. (2018).
- 943 38. Devlin, J., Chang, M.-W., Lee, K. & Toutanova, K. Bert: Pre-training of deep bidirectional  
944 transformers for language understanding. *arXiv preprint arXiv:1810.04805* (2018).
- 945 39. Li, W., Wong, W.H. & Jiang, R. DeepTACT: predicting 3D chromatin contacts via bootstrapping  
946 deep learning. *Nucleic acids research* **47**, e60-e60 (2019).
- 947 40. Chor, B., Horn, D., Goldman, N., Levy, Y. & Massingham, T. Genomic DNA k-mer spectra:

- 948 models and modalities. *Genome biology* **10**, 1-10 (2009).
- 949 41. Zhou, Q., Chipperfield, H., Melton, D.A. & Wong, W.H. A gene regulatory network in mouse  
950 embryonic stem cells. *Proceedings of the National Academy of Sciences* **104**, 16438-16443  
951 (2007).
- 952 42. Sharov, A.A. et al. Identification of Pou5f1, Sox2, and Nanog downstream target genes with  
953 statistical confidence by applying a novel algorithm to time course microarray and genome-  
954 wide chromatin immunoprecipitation data. *BMC genomics* **9**, 1-19 (2008).
- 955 43. Raz, R., Lee, C.-K., Cannizzaro, L.A., d'Eustachio, P. & Levy, D.E. Essential role of STAT3 for  
956 embryonic stem cell pluripotency. *Proceedings of the National Academy of Sciences* **96**, 2846-  
957 2851 (1999).
- 958 44. van den Berg, D.L. et al. An Oct4-centered protein interaction network in embryonic stem cells.  
959 *Cell stem cell* **6**, 369-381 (2010).
- 960 45. Zhang, J. et al. The oncogene Etv5 promotes MET in somatic reprogramming and orchestrates  
961 epiblast/primitive endoderm specification during mESCs differentiation. *Cell death & disease*  
962 **9**, 224 (2018).
- 963 46. Fang, L. et al. GRNdb: decoding the gene regulatory networks in diverse human and mouse  
964 conditions. *Nucleic acids research* **49**, D97-D103 (2021).
- 965 47. Han, H. et al. TRRUST v2: an expanded reference database of human and mouse transcriptional  
966 regulatory interactions. *Nucleic acids research* **46**, D380-D386 (2018).
- 967 48. Willett, R. et al. TFEB regulates lysosomal positioning by modulating TMEM55B expression  
968 and JIP4 recruitment to lysosomes. *Nature communications* **8**, 1580 (2017).
- 969 49. Bernstein, B.E. et al. The NIH roadmap epigenomics mapping consortium. *Nature*  
970 *biotechnology* **28**, 1045-1048 (2010).
- 971 50. Kulakovskiy, I.V. et al. HOCOMOCO: towards a complete collection of transcription factor  
972 binding models for human and mouse via large-scale ChIP-Seq analysis. *Nucleic acids research*  
973 **46**, D252-D259 (2018).
- 974 51. Heinz, S. et al. Simple combinations of lineage-determining transcription factors prime cis-  
975 regulatory elements required for macrophage and B cell identities. *Molecular cell* **38**, 576-589  
976 (2010).
- 977 52. He, K., Zhang, X., Ren, S. & Sun, J. in Proceedings of the IEEE conference on computer vision

- 978                   and pattern recognition 770-778 (2016).
- 979    53.    Chen, S. et al. OpenAnnotate: a web server to annotate the chromatin accessibility of genomic
- 980                   regions. *Nucleic Acids Research* **49**, W483-W490 (2021).

## 981 **Supplementary Materials**

982 Fig. S1. Three data partitioning strategies for model training and testing.

983 Fig. S2. EpiGePT's performance in predicting DNase-seq and other epigenetic signals.

984 Fig. S3. Performance of EpiGePT and baseline methods on chromatin states classification,  
985 multiple epigenomic profiles prediction and causal variants classification.

986 Fig. S4. Ablation analysis of the EpiGePT model.

987 Fig. S5. Case application of the EpiGePT-online.

988 Fig S6. Model architecture of EpiGePT for multiple epigenomic signals prediction.

989 Fig. S7. The fine-tuning performance of the EpiGePT model on predicting potential enhancer-  
990 promoter regulatory networks.

991 Fig. S8. The performance (auROC) of attention score of EpiGePT in distinguishing regulatory  
992 element-gene pairs at different distance ranges.

993 Text S1. Data splitting strategy for model training.

994 Text S2. System design and implementation of the web server.

995 Text S3. Running time of the EpiGePT and baseline methods.

996 Text S4. Implementation of Enformer model and Enformer+.

997 Table S1. The information of DNase-seq bam file across 129 biosamples from the ENCODE  
998 project.

999 Table S2. The information of RNA-seq tab-separated values (tsv) file across 129 biosamples  
1000 from the ENCODE project.

1001 Table S3. The information of DNase-seq, CTCF and other six Histone markers bam file across  
1002 28 cell lines or tissues from the ENCODE project.

1003 Table S4. The information of RNA-seq tab-separated values (tsv) file across 28 cell lines or  
1004 tissues from the ENCODE project.

1005 Table S5. The preprocessed expression data of 711 human transcription factors from the  
1006 ENCODE project across 129 biosamples.

1007 Table S6. The preprocessed expression data of 711 human transcription factors from the  
1008 ENCODE project across 28 cell lines or tissues.

1009 Table S7. The order and names of epigenomes of the expression matrices across 56 epigenomes

1010 from the ROADMAP project.

1011 Table S8. The preprocessed expression data of 642 human transcription factors across 56

1012 epigenomes from the ROADMAP project.